Coupled Neutronics-Thermalhydraulics LOCA Analysis

by

B. Rouben
Manager, Reactor Core Physics Branch
AECL

Presented at Chulalongkorn University
Bangkok, Thailand, 1997 December

Abstract

A coupled neutronics-thermalhydraulics analysis of a loss-of-coolant accident (LOCA) in CANDU is presented. The calculation is performed with the *CERBERUS (spatial-kinetics) module of the finite-core code RFSP, coupled to the thermalhydraulics code FIREBIRD. The power pulse which results from the hypothetical LOCA is assumed terminated by Shutdown System 1 (SDS-1). The calculational methodology and the physics model used in the LOCA analysis are detailed. The significant parameters which govern the results of the calculation are discussed.

Table of Contents

1. Introduction
2. The Spatial-Kinetics Methodology in *CERBERUS
2. Analysis Methods and Assumptions
   - 2.1 Time-Dependent Neutron-Diffusion Equation
   - 2.2 Improved Quasi-Static (IQS) Method
   - 2.3 Two-Tiered Scheme of Time Intervals
3. Lattice Properties and the History-Based Method
4. Neutronic-Thermalhydraulic Coupling
5. LOCA Simulated
   - 5.1 RFSP Neutronics Model
   - 5.2 Prevailing and Simulated Initial Conditions
     - 5.2.1 Moderator Poison
     - 5.2.2 Reactor Power
     - 5.2.3 Coolant Purity
     - 5.2.4 Pressure-Tube Creep
   - 5.3 FIREBIRD Thermalhydraulics Model
   - 5.4 Shutdown-System Actuation
6. Results
   - 6.1 Steady State
   - 6.2 Detector Response
   - 6.3 Thermalhydraulic Behaviour
   - 6.4 Neutronic Behaviour
   - 6.5 Fuel Enthalpy
7. Summary

Figures

2.1 Two-Tiered Numerical Scheme in Time Used in the *CERBERUS Methodology
3.1 Infinite Multiplication Constant of 37-Element Fuel as a Function of Irradiation
5.1 PHTS Circuit Showing Location of Pump-Suction Break
5.2 Channel Groups in Thermalhydraulics Model
5.3 Reactor Elevation Showing Shutoff Rods
5.4 Top View of Reactor Showing Shutoff-Rod Positions
5.5 Contour Map of Steady-State Channel-Power Distribution
6.1 Coolant-Density Transients in the Various Channel Groups
6.2 Channel Voiding Transients
6.3 Loop Void Fractions
6.4 Flow in Channel Groups 1-5
6.5 Header-Pressure Transients in Broken Loop
6.6 Break-Discharge-Flow Transient
6.7 Total System Reactivity (Positive Values)
6.8 Total System Reactivity Through the Transient
6.9 Power transients for Channel Groups 1-5
6.10 Total Reactor Power and Loop Powers
6.11 Power Pulse for Bundle with Highest Deposited Energy

Tables

1 Delayed-Neutron Data
2 Times at which SDS-1 Detectors Reached Their Setpoints
3 Total System Reactivity
4 Total Reactor Power and Loop Powers
5 Induced Side-to-Side Power Tilt
6 Power Pulse for Bundle with Highest Deposited Energy

1. Introduction

The major finite-core computer program used for the design and analysis of CANDU reactors is RFSP (Reactor Fuelling Simulation Program). The physics models used with RFSP are the most detailed and realistic representations available for the CANDU core.

The early versions of RFSP were limited to steady-state calculations. Subsequently, a spatial-kinetics module (*CERBERUS) was incorporated. The calculational methodology in the *CERBERUS module is based on the Improved Quasi-Static method for the solution of the time-dependent equation. RFSP therefore now provides the most sophisticated tools and the most realistic physics models for the analysis of fast neutronic transients.

The main application of spatial kinetics to CANDU analysis is in the simulation of the power pulse associated with loss-of-coolant accidents (LOCA). For this purpose, the *CERBERUS module is coupled to thermalhydraulics codes, such as FIREBIRD-III and CATHENA, which model the primary heat-transport system.

Inherent in the RFSP modelling of the core are bundle-specific lattice properties, functions of the bundle fuel irradiation (burnup). In addition, for kinetics calculations, the history-based local-parameter methodology is used, where bundle-specific lattice properties are calculated consistent with locally appropriate values of lattice parameters, such as coolant density, coolant temperature, absolute flux (power), and fuel temperature. The history-based methodology facilitates individual lattice calculations for **each** fuel bundle at **each time** in the transient. Bundle-specific delayed-neutron fractions are also used.

The methodology for coupled neutronics-thermalhydraulics calculations is illustrated here with a sample calculation of a LOCA from a specific instant in the operating history of a CANDU-6 reactor, i.e., an instantaneous flux distribution - specifically, at Full-Power Day (FPD) 2844 in the core operating history. The LOCA is assumed to be initiated by a 100% pump-suction-pipe break, with the pre-accident reactor assumed to be at 103% FP, with a boron concentration of 0.625 ppm in the moderator (corresponding to an excess core reactivity of 5 milli-k due to overfuelling) and equilibrium levels of saturating fission products. The resulting power pulse is assumed terminated by Shutdown System 1 (SDS-1).

2. The Spatial-Kinetics Methodology in *CERBERUS

2.1 Time-Dependent Neutron-Diffusion Equation

The basic methodology used is the time-dependent neutron-diffusion equation, solved in 3 spatial dimensions and 2 energy groups.

In fast transients, delayed-neutron effects are extremely important. We assume the delayed-neutron precursors are represented by 6 distinct groups, or 15 groups if the photoneutrons are treated separately from the delayed neutrons originating in the fuel. We shall denote the number of delayed-neutron groups by G.

In matrix notation, the time-dependent neutron diffusion equation in two energy groups can be written

$$\left(-M+F_p\right)\phi(\vec{r},t)+\sum_{g=1}^{G}\lambda_g C_g(\vec{r},t)\begin{pmatrix}1\\0\end{pmatrix}=\left(\frac{1}{v}\right)\frac{\partial\phi(\vec{r},t)}{\partial t} \tag{2.1}$$

where the two-group time-dependent neutron flux is represented by the vector

$$\phi(\vec{r},t)=\begin{pmatrix}\phi_1(\vec{r},t)\\ \phi_2(\vec{r},t)\end{pmatrix} \tag{2.2}$$

and the group inverse velocities are in the matrix

$$\left(\frac{1}{v}\right)=\begin{pmatrix}\frac{1}{v_1} & 0\\ 0 & \frac{1}{v_2}\end{pmatrix} \tag{2.3}$$

The operators in Eq. (2.1) are as follows.

M is the leakage, absorption, and scattering matrix:

$$M=\begin{pmatrix}-\vec{\nabla}\cdot D_1\vec{\nabla}+\Sigma_{a1}(\vec{r},t)+\Sigma_{1\to2}(\vec{r},t) & 0\\ -\Sigma_{1\to2}(\vec{r},t) & -\vec{\nabla}\cdot D_2\vec{\nabla}+\Sigma_{a2}(\vec{r},t)\end{pmatrix} \tag{2.4}$$

and F_p is the prompt-neutron-production matrix:

$$F_p\equiv\left(1-\beta(\vec{r},t)\right)F_T=\begin{pmatrix}0 & \frac{\left(1-\beta(\vec{r},t)\right)\nu\Sigma_f(\vec{r},t)}{k_0}\\ 0 & 0\end{pmatrix} \tag{2.5}$$

where k_0 is the initial multiplication constant of reactor. Its presence as a divisor of $\nu\Sigma_f$ ensures that the transient simulated starts from a steady state initially. Note also that k_0 is **not** related to the time-dependent dynamic reactivity ρ which will be calculated through the transient.

Note that the production matrix F_p acts on the thermal-neutron group only, i.e., all neutrons are assumed born from thermal-neutron-induced fission (or, fast fissions are "lumped" with thermal fissions).

$\beta(\vec{r},t)$ is the total delayed fraction at position $(\vec{r},t)$, the sum of the partial delayed fractions for the G delayed groups:

$$\beta=\sum_{g=1}^{G}\beta_g \tag{2.6}$$

and $C_g(\vec{r},t)$ is the space-time concentration of group-g delayed-neutron precursor, whose decay constant is λ_g.

The precursor concentration for each delayed-group g satisfies the balance equation which contains the production term from fission and the loss term from radioactive decay:

$$\frac{\partial}{\partial t}C_g(\vec{r},t) = \beta_g(r)\frac{\nu\Sigma_f(\vec{r},t)}{k_0}\phi_2(\vec{r},t) - \lambda_g C_g(\vec{r},t) \tag{2.7}$$

2.2 Improved Quasi–Static (IQS) Method

The calculational procedure in *CERBERUS is based on the Improved Quasi-Static (IQS) method. The flux is (without loss of generality) factorized into a space-independent amplitude A and space-and-time-dependent shape function ψ:

$$\phi(\vec{r},t) = A(t)\psi(\vec{r},t) \tag{2.8}$$

The amplitude is normalized to an initial value of unity:

$$A(0) = 1 \tag{2.9}$$

The principle of the IQS method is to cast most of the time dependence of the flux into the *amplitude*. This is achieved by ensuring that an integral in the shape function remains constant in time:

$$\int\left[\frac{1}{v_1}\phi_1^*(\vec{r})\psi_1(\vec{r},t) + \frac{1}{v_2}\phi_2^*(\vec{r})\psi_2(\vec{r},t)\right]d\vec{r} = K \tag{2.10}$$

In this integral, as in all integrals in the IQS method, a weighting function (vector) equal to the initial adjoint flux $\begin{pmatrix}\phi_1^*(\vec{r})\\ \phi_2^*(\vec{r})\end{pmatrix}$ (also known as the importance function). The adjoint is used because it has the property that it makes the value of reactivity a stationary function of the flux shape, thus minimizing its sensitivity to possible numerical (e.g., round-off) errors in calculating the flux.

We now substitute the form (2.8) into Eqs. (2.1) and (2.7) to derive equations for the shape function ψ and the precursor concentrations C_g. We get

$$\left(-M + F_p\right)\psi(\vec{r},t) + \frac{1}{A(t)}\sum_{g=1}^{G}\lambda_g C_g(\vec{r},t)\begin{pmatrix}1\\0\end{pmatrix} = \left(\frac{1}{v}\right)\frac{\dot{A}(t)}{A(t)}\psi(\vec{r},t) + \frac{\partial\psi(\vec{r},t)}{\partial t} \tag{2.11}$$

and

$$\frac{\partial}{\partial t}C_g(\vec{r},t) = \beta_g(\vec{r})\frac{\nu\Sigma_f(\vec{r},t)}{k_0}A(t)\psi_2(\vec{r},t) - \lambda_g C_g(\vec{r},t) \tag{2.12}$$

Compare Eq. (2.11) to the time-independent neutron-diffusion equation:

$$\left(-M + F_p\right)\psi(\vec{r},t) = 0 \tag{2.13}$$

We can see that Eq.(2.11) is similar, except that it has extra terms in the amplitude and in the precursor concentrations. Eq. (2.13) is solved in its finite-difference form, in the same manner as Eq. (2.11). Since the flux is calculated at typically tens of thousands of mesh points in the finite-difference model, the solution requires an iterative scheme.

The equation for the amplitude is obtained by integrating Eq.(2.11) over the core, once again using the steady-state adjoint as weighting factor. When we do this, we get a point-kinetics-like equation:

$$\dot{A}(t) = \frac{\left(\rho(t) - \beta_{eff}\right)}{\Lambda(t)} A(t) + \frac{1}{K} \sum_{g=1}^{G} \lambda_g \eta_g(t) \tag{2.14}$$

where the parameters ρ, β_{eff}, Λ, and η_g have the following significance and are computed as core integrals.

ρ is the dynamic reactivity:

$$\rho(t) = 1 - \frac{\left\langle \phi^*(\vec{r}), M\psi(\vec{r},t) \right\rangle}{\left\langle \phi^*(\vec{r}), F_T\psi(\vec{r},t) \right\rangle} \tag{2.15}$$

$$= 1 - \frac{\text{losses}}{\text{production}}$$

Λ is the prompt-neutron lifetime:

$$\Lambda(t) = \frac{K}{\left\langle \phi^*(\vec{r}), F_T\psi(\vec{r},t) \right\rangle} \tag{2.16}$$

β_{eff} is the effective total delayed-neutron fraction:

$$\beta_{eff} \equiv \sum_{g=1}^{G} \beta_{g,eff} = \sum_{g=1}^{G} \frac{\left\langle \phi^*(\vec{r}), \beta_g F_T\psi(\vec{r},t) \right\rangle}{\left\langle \phi^*(\vec{r}), F_T\psi(\vec{r},t) \right\rangle} \tag{2.17}$$

The η_g values are the adjoint-weighted integrated precursor concentrations:

$$\eta_g(t) = \int \phi_1^*(\vec{r}) C_g(\vec{r},t) d\vec{r} \qquad \text{g=1,...G} \tag{2.18}$$

By integrating Eq. (2.11) over the core in a similar manner, with the adjoint as weighting function, we find that the integrated precursor concentrations satisfy the balance equations

$$\dot{\eta}_g(t) = K \frac{\beta_{g,eff} A(t)}{l^*(t)} - \lambda_g \eta_g(t) \tag{2.19}$$

The IQS calculational methodology is now complete. The original time-dependent neutron-diffusion equation is equivalent to a coupled system of equations for the shape function ψ, the amplitude A, and both the space-dependent and the integrated precursor concentrations C_g and η_g. This coupled system consists of the space- and time-dependent differential equations (2.11), (2.12), and the equations (2.14) and (2.19) which are dependent on time only. This system depends on the integrated quantities defined in (2.15)-(2.18).

2.3 Two-Tiered Scheme of Time Intervals

While we have replaced a single equation by a system of coupled equations, the scheme we have obtained has the advantage that most of the time dependence has been cast into the amplitude. Consequently, the space-dependent equation for the shape function, which requires a much greater computational effort to solve than the point-kinetics-like equations for the amplitude, can be solved much less frequently (through the transient). In this way, the IQS method significantly reduces the overall computational effort.

*CERBERUS thus employs a two-tiered strategy in the time variable:

- solve the shape equation only at relatively large time steps (**macro intervals**), and
- solve the point-kinetics-like equations for the amplitude and integrated precursor concentrations at small time steps (**micro intervals**).

This two-tiered scheme in time is illustrated in Figure 2.1.

We start by selecting the points in time in the transient, $t_1 = 0$, t_2, t_3,. . ., at which we wish to calculate the shape function ψ. These define the macro intervals. For typical CANDU transients, the following macro intervals are generally found to be appropriate:

- at the start of a LOCA, before shutdown-system actuation, 50-100 ms;
- during shutdown-system action, until full system insertion, the time interval it takes for the shutdown system (tip of shutoff rods or leading edge of poison along the injecting nozzle) to travel an additional lattice pitch; this time varies during the action of the shutdown system but is typically of the order of 10-50 ms;
- following shutdown-system full insertion, larger intervals in the range of a several tenths of a second to a few seconds.

The starting point of the process is the solution of the pre-event (i.e., $t_1 = 0$) steady-state problem. The solution of the shape equation (2.12) then follows recursively from one ("macro") point in time to the next, t_j to t_{j+1}. However, since the amplitude and its rate of change appear in Eq. (2-12), this requires that equations (2.14) and (2.19) be solved over micro intervals within the macro interval. In fact, the coupling of all the equations forces the **iterative solution of the entire set** over each macro interval, until self-consistency is attained in each quantity: flux shape, amplitude, reactivity, precursors.

In *CERBERUS, the calculation at a given macro time step t_j in the transient is called a "**case**", and the cases are numbered:

- Case 1 is the initial steady state at $t_1 = 0$.
- Case 2 is the steady-state adjoint, also at $t_1 = 0$; this is needed to calculate all subsequent core integrals.
- Cases 3, 4, 5, ... are the time-dependent cases at times t_2, t_3, t_4, etc.

3. Lattice Properties and the History-Based Method

The fuel-management code RFSP is the major finite-core computer program for the design and analysis of CANDU reactors. The core models used with RFSP are the most accurate and realistic. While RFSP was initially only a steady-state code, these attributes ensured that its extension to a kinetics capability would be a natural development. This development took the form of the *CERBERUS module, whose mathematical basis is described in the previous section.

RFSP incorporates within it the cell code POWDERPUFS-V, which evaluates the nuclear properties (cross sections) of the lattice. POWDERPUFS-V is a semi-empirical code, based on research-reactor measurements on heavy-water-moderated lattices. The mathematical framework of POWDERPUFS-V is quite simple, and its execution time is a very small fraction (about 1/200th) that of a transport code such as WIMS-AECL.

The lattice properties calculated by the cell code are the basic data for use in any finite-reactor calculation. For a given lattice and fuel geometry, the major determinant of the lattice properties is the fuel irradiation. In this context, Figure 3.1 shows the variation with irradiation of k_∞, the "infinite-lattice" multiplication constant, for 37-element natural-uranium fuel irradiated under nominal conditions. In addition, the void reactivity is also a function of fuel irradiation: it is of the order of 15 mk for fresh fuel, and 10 mk for mid-burnup fuel. These factors demonstrate how important it is to model the spatial distribution of fuel irradiation in the RFSP core model.

Given the lattice properties, RFSP tackles the finite-core problem. For steady-state problems, RFSP solves the time-independent neutron-diffusion equation. Two types of models are essentially available here:

- the time-average model, which is intended to provide an "average" picture of the core configuration over the long term. In this model, each bundle does not have a single irradiation value, but instead is represented by a range of irradiations which the fuel experiences at that location. This model does not include the "fuelling ripple" associated with the discrete, daily refuelling operations;
- the instantaneous ("snapshot") model, representing the picture of the core on some specific day in the reactor's operating history. This model explicitly includes the fuelling ripple due to the sequence of refuelling operations leading to the specific day being modelled.

In both models, lattice properties are bundle-specific, because the values of irradiation (burnup) are individual to each fuel bundle in core. In the snapshot model, some channels have been refuelled very recently, others have not been visited for a long time, and are nearing the time when they will be refuelled once again. Thus, the fuel irradiation in the core ranges from 0 (or near 0) to values near the expected exit value. Since irradiation is the most important parameter determining the nuclear properties, the lattice properties must be evaluated separately for each bundle.

However, other parameters, such as the absolute local flux value, the fuel temperature, the coolant density, etc., also have an impact on the lattice properties, and these parameters are not uniform through the core. It is therefore desirable that lattice properties be calculated with "local-parameter" methodologies which capture the local variation in lattice conditions. The most accurate methodology available in RFSP is the "history-based" method: at each successive snapshot in the reactor's operating history (i.e., each burn step), individual POWDERPUFS-V lattice calculations for each bundle to update its properties based on the bundle's changing irradiation and the local

parameters at the bundle's location **at that time**. Thus, true to its name, the history-based method reflects changes due to the local **history** of each bundle. This is particularly important in simulations of hypothetical accidents such as LOCAs, where major space-dependent changes in lattice properties are taking place.

Thus, the *CERBERUS module of RFSP, developed specifically to analyze fast transients such as LOCAs, is designed to function within the context of the history-based methodology. This is well suited to calculations of the "perturbation" type, where changes in the basic lattice properties due to sudden events or accidents must be modelled, and especially when these changes are likely to vary widely across the core.

Note however that in view of the thousands of lattice calculations required (there are 4560 fuel bundles in the CANDU 6), the history-based methodology is practical only if the lattice code executes sufficiently rapidly: the advantage of POWDERPUFS-V is that the cell calculations for all 4560 bundles take only about one minute on an HP workstation.

Because the number of delayed neutrons from plutonium fissions is smaller than that from uranium fissions, the delayed-neutron fractions needed for the kinetics calculations depend on the isotopic nuclide concentrations in the fuel, i.e. they are also irradiation dependent. For *CERBERUS, bundle-specific delayed-neutron fractions are calculated within the history-based method.

4. Neutronic-Thermalhydraulic Coupling

In the LOCA application, the driving feature is the coolant-density transient. In a large break, this evolves rapidly in time. There are also significant variations in the density transient in space, since the voiding will initially be in the critical pass of the broken loop, and even within that pass it will depend on the local power and on the channel's position in the core.

Therefore, to capture the effect of the rapid changes in coolant density on the lattice properties, the latter must be re-evaluated at each "flux-shape" time step, using densities imported from a thermalhydraulics calculation. Since the local power also drives the voiding to some extent, the *CERBERUS module has been coupled to a thermalhydraulics calculation (done, e.g., by a code such as FIREBIRD or CATHENA).

A detailed thermalhydraulics model of the primary heat-transport system must be assembled. Even with the increased power of modern computers, it is still not practical in thermalhydraulics models to represent every channel in the core individually. However, a fair degree of detail can be obtained by subdividing the fuel channels into a reasonable number of thermalhydraulics groups, each representing channels with similar expected density transient.

The coupled neutronics-thermalhydraulics calculation then proceeds through the transient in one "go-through" as follows. RFSP calculates the flux and power distributions (including fission–product decay power) at the discrete ("flux-shape") macro time steps described earlier. At each macro time step, RFSP sums up the bundle powers for each of the channel groups used in the thermalhydraulics model. The thermalhydraulics code then uses this information to compute coolant densities, fuel temperatures and coolant temperatures for the next macro time interval in the transient. In this way the LOCA simulation steps through the transient, alternating between the neutronics and thermalhydraulics components of the calculation.

5. LOCA Simulated

The LOCA transient simulated here to illustrate the methodology is a hypothetical 100% break in the pump-suction pipe of pump 4, located in loop 2, at the pressurizer end of a CANDU 6 (see Figure 5.1). The break size corresponding to this break is about 0.308 m^2. The critical core pass is the pass between reactor headers HD8 and HD5.

The power pulse is assumed to be terminated by SDS-1. This is in fact the reason for assuming the pipe break is in loop 2. For SDS-1 action, this is more conservative than a break in loop 1: the SDS-1 ion chambers being on the loop-1 side of the calandria, their response will be slower to a break in loop 2.

5.1 RFSP Neutronics Model

The LOCA was assumed to occur at a particular day, FPD 2844. in the CANDU 6 operating history. A "history-based" snapshot model corresponding to FPD 2844 was used as the basis of the simulation. The core was in a nominal configuration at full power.

Note: some of the figures presented in the discussion show two sets of results:

- those obtained with the snapshot model, using RFSP (*CERBERUS module); these are labelled "RFSP simulation", and
- those obtained with an earlier, "self-standing" CERBERUS code (not within RFSP), using the same IQS method, but with a crude version of the time-average model instead of a snapshot model; these are labelled "CERBERUS simulation".

5.2 Prevailing and Simulated Initial Conditions

This section discusses the pre-event core conditions prevailing in the core on the FPD selected, and how some of these were modified in the simulation for reasons of conservatism.

5.2.1 Moderator Poison

FPD 2844 in the operating history was selected because it represented a nominal core configuration at full power, following a period with a high rate of refuelling. As a result, the core had about 0.4 ppm of boron in the moderator, corresponding to an excess reactivity of about 3 milli-k. However, in the simulation the moderator poison concentration was for conservatism increased to 0.625 ppm of boron, corresponding to 5 milli-k of excess reactivity, the maximum amount allowed by the station operating procedures. The presence of moderator poison increases the void reactivity and therefore the severity of the power pulse.

5.2.2 Reactor Power

Although the reactor was operating at full power on FPD 2844, an uncertainty of 3% in the measured power was assumed in the simulation. Therefore the initial power was increased to 103% FP (= 1.03*2061.4 = 2123.2 MW). The higher power would increase the voiding rate and consequently the severity of the power pulse. It would also increase the initial fuel temperature (and therefore the initial stored energy), and the energy added to the fuel for the same ***relative*** power pulse.

5.2.3 Coolant Purity

The coolant purity at FPD 2844 was 98.89 atom % D_2O. The purity was downgraded in the simulation, to artificially increase the void reactivity, to account for a possible underestimation of the void reactivity by the cell code POWDERPUFS-V. A lower coolant purity results in greater parasitic absorption when the coolant is present, and therefore a greater reactivity addition when the coolant is voided. The value used in the simulation was 94.26 atom %, corresponding to the **minimum** operational purity allowed at the station, 97.15 atom %, and an assumed void-reactivity uncertainty of 1.6 mk.

5.2.4 Pressure-Tube Creep

Pressure-tube radial creep was incorporated in the model. Although FPD 2844 corresponds to a period of operation of 9 years at 90% capacity factor, the simulation assumed 20 years of creep at a 90% capacity factor. Four different values of creep were used, corresponding to two radial regions (inner and outer cores) and two axial core regions.

5.3 FIREBIRD Thermalhydraulics Model

The thermalhydraulics computer code used was FIREBIRD.

The thermalhydraulics circuit was divided into 8 channel groups, as shown in Figure 5.2. The greatest detail and subdivision was used in the critical pass, the one downstream of the break in the broken loop. This pass features the fastest density transients. Here five thermalhydraulics groups (1-5) were selected, to distinguish between the high-power and low-power channels in the inner and outer regions of the core, and within each region to distinguish between the different elevations of channels. The non-critical pass of the broken loop features much slower density transients, and a single thermalhydraulics group (channel group 6) was used to model the 95 channels. Similarly in each of the two passes of the intact loop (channels groups 7 and 8).

The core region in each channel group in the critical pass (i.e. channel groups 1 to 5) was represented by 12 FIREBIRD nodes, corresponding to one axial bundle plane each. For channel groups 6 to 8, where core voiding was not significant, a 4-node axial representation was used.

5.4 Shutdown-System Actuation

The hypothetical LOCA transient was assumed terminated by SDS-1 acting alone.

Figure 5.3 shows a face view of the core with the shutoff rods fully inserted. Figure 5.4 is a top view of the reactor, showing the shutoff-rod positions. In order to accommodate the shutoff rods in the model mesh lines, the RFSP model makes some conservative assumptions about the shutoff rod length. The length is reduced from the actual active length to 18 lattice pitches for the long rods (a shortening of almost one lattice pitch), and to 17 lattice pitches for the short rods.

In the LOCA analysis, two of the 28 shutoff rods are assumed to be inoperative. The rods which leave the **least effective** set of 26 rods operative are assumed absent; these are rods SOR01 and SOR05. From Figure 5.4 it may be seen that assuming these rods are inoperative leaves a large corner of the reactor not covered by the shutdown system.

The reactor shutdown system is actuated by the reactor protection system. The **neutronic** components of the protection system consist of out-of-core ion chambers and in-core Regional Overpower Protection (ROP) detectors. There are also non-neutronic, i.e., process, components of the protection system, but these were not simulated here.

The protection system actuates the shutdown system on the **first** trip signal encountered. The simulation however ignored the first trip signal and assumed instead the **second** (i.e., the **backup** trip signal).

The *TRIPDPG module of RFSP computes the shutdown-system actuation time. *TRIPDPG models all the detectors and the ion chambers and their electronics. The trip logic is triplicated, and although the tripping of two logic channels is sufficient to trip the entire system, the simulation required all three logic channels to trip before actuating the shutdown system.

6. RESULTS

6.1 Steady State

The FIREBIRD steady-state assumed two-phase flow at 103% FP with an outlet-header quality of 3.6%. The reactor outlet header (ROH) pressures connected to the pressurizer were set at 9.99 MPa(a).

The initial global flux distortions were very small. A contour map of the channel powers across the core is given in Figure 5.5. Local power variations in the instantaneous model are expected, as they are due to the refuelling ripple about the time-average power distribution.

The delayed-neutron data calculated in the steady state case is summarized in Table 1, showing the average values and the variations for the 6 delayed-neutron groups. The total delayed fraction β in steady state was found to be about $(5.87 \pm 0.92) \times 10^{-3}$, where the $\pm$ value quoted is the standard deviation across the core. It is clear that the spatial variation in the delayed fraction is substantial.

6.2 Detector Response

The times at which the SDS-1 detectors reached their setpoints are listed in Table 2. The SDS-1 backup trip signal was the rate-of-log-power signal. The time of actuation of SDS-1 was 495 ms after the break. Taking into account the time it takes for the shutoff rods to drop from their parked position, their time of entry into the core was 0.883 s after the break. [A loop-1 break would have been detected earlier by the SDS-1 ion chambers and would have led to an earlier SDS-1 actuation time.]

6.3 Thermalhydraulic Behaviour

From a thermalhydraulics point of view, void reactivity depends on the initial amount of coolant in the core, and also on the voiding rate. The larger the coolant mass, the larger the amount of coolant lost and the larger the core void reactivity. In addition, a faster voiding rate results from an initial condition with some coolant boiling at the core exit. This is the reason for assuming an initial power greater than design full power.

Figure 6.1 shows the (flux-square-weighted) average coolant densities in channel groups 1 to 5 of the critical pass and in channel groups 6 to 8 of the other core passes.

The channel voiding transient is shown in Figure 6.2. Figure 6.3 shows the total void-fraction transients in the intact and the broken loops (loops 1 and 2, respectively). The initial void fraction in each loop is about 0.1, corresponding to the outlet boiling. The flows in channel groups 1 to 5 are shown in Figure 6.4. Figure 6.5 shows the header-pressure transients in the broken loop. The break-discharge-flow transient is shown in Figure 6.6.

6.4 Neutronic Behaviour

The initial (positive) segment of the variation of core reactivity is shown in Figure 6.7. Figure 6.8 shows the total reactivity for the entire transient (also in Table 3). The shutoff rods begin to "bite" into the reactivity as soon as they enter the core. The reactivity reaches a peak positive value of 4.08 milli-k at 0.883 s after the break. At that time the channels of the critical pass have almost completely voided.

The reactivity becomes negative very quickly as the shutoff rods continue to drop into the core. The rods reach full insertion at about 2.1 s. Thereafter, the flux shape does not change appreciably, and the reactivity levels out at approximately -76 milli-k.

Figure 6.9 shows the power transients for channel groups 1 to 5, at mid-axial location. Table 4 gives the relative powers of the entire reactor, the broken loop (loop #2 - low-x half in the reactor model) and the intact loop (high-x half). Also shown are the relative powers for the top and bottom halves and the two axial halves. The total power and loop powers are plotted in Figure 6.10. Because of the asymmetric coolant voiding, the broken-loop power rises faster than the intact-loop power, resulting in a side-to-side power tilt of about 14% before the shutoff rods enter the core (Table 5).

6.5 Fuel Enthalpy

The bundle which had the highest energy deposited to 5 s was bundle P05-7. The power versus time for this bundle is tabulated in Table 6 and graphically in Figure 6.11. In the RFSP transient, the bundle reaches its peak power at 1.229 s; the increase over its initial power (827.6 kW) is a factor of 3.65.

Over 5 s, the total energy added to the bundle was 3.557 MW·s, or 4.298 initial-power-seconds. Assuming the same *relative* power pulse were experienced by a hypothetical bundle initially at the licensing limit of 935 kW, the total energy content (initial stored energy + energy deposited by the power pulse) of fuel in the hot pin of the hypothetical bundle would be 589.6 J/g. This is 250.4 J/g below a conservative limit of 840 J/g for fuel break-up; the margin is 29.8%.

7. Summary

The spatial-kinetics capability of the RFSP code has been illustrated by means of the simulation of a hypothetical LOCA transient. The calculation featured coupling of the RFSP neutronics with a thermalhydraulics (FIREBIRD) model.

The LOCA was calculated for an instantaneous (snapshot) model of the core. However, many reactor conditions were artificially changed to increase the severity of the power pulse, for conservatism. The snapshot RFSP model is a very detailed representation of the core. The physical properties of the lattice, including the delayed-neutron data, are bundle-specific in the calculation.

Prior to the development of the *CERBERUS spatial-kinetics module of RFSP, the modelling of the core was cruder, with lattice properties assumed homogeneous (or averaged) over large regions of the core. The *CERBERUS module allows neutron-kinetics analysis to be performed with the most sophisticated reactor models. It also allows LOCA analysis to be performed for arbitrary snapshots of the core, situations which could not previously be handled.

Table 1. Void Reactivity vs Coolant Purity at 1.80 n/kb (Reaction-Rate Averaged)

Coolant Purity (atom%)	Reactivity (milli-k) .80640 g/cm^3	Reactivity (milli-k) voided	Dr (mk)	Difference from Reference (mk)	slope (mk/atom%)
99.8	2.38485E-02	3.34682E-02	9.620	-0.739	-
98.929			10.080		
98.4	2.27996E-02	3.31587E-02	10.359	0.000	-0.5282
97.0	2.17627E-02	3.28594E-02	11.097	0.738	-0.5269
95.0	2.03020E-02	3.24498E-02	12.148	1.789	-0.5255
92.5	1.85114E-02	3.19688E-02	13.457	3.098	-0.5238
90.0	1.67611E-02	3.15233E-02	14.762	4.403	-0.5220
88.0	1.53931E-02	3.11935E-02	15.800	5.441	-0.5191
85.0	1.34037E-02	3.07484E-02	17.345	6.986	-0.5148

Figure 1. POWDERPUFS-V Void Reactivity vs Coolant Purity

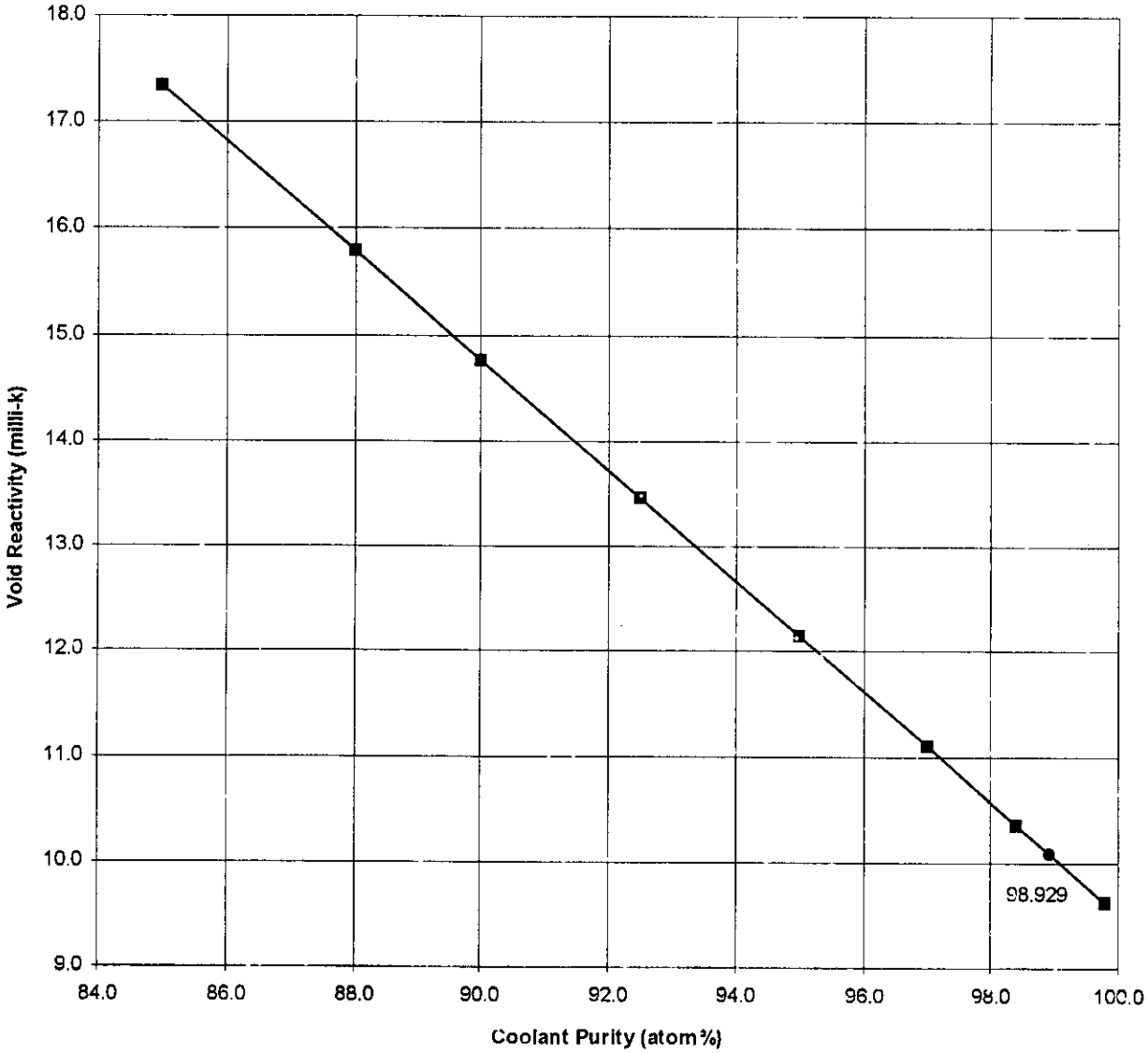

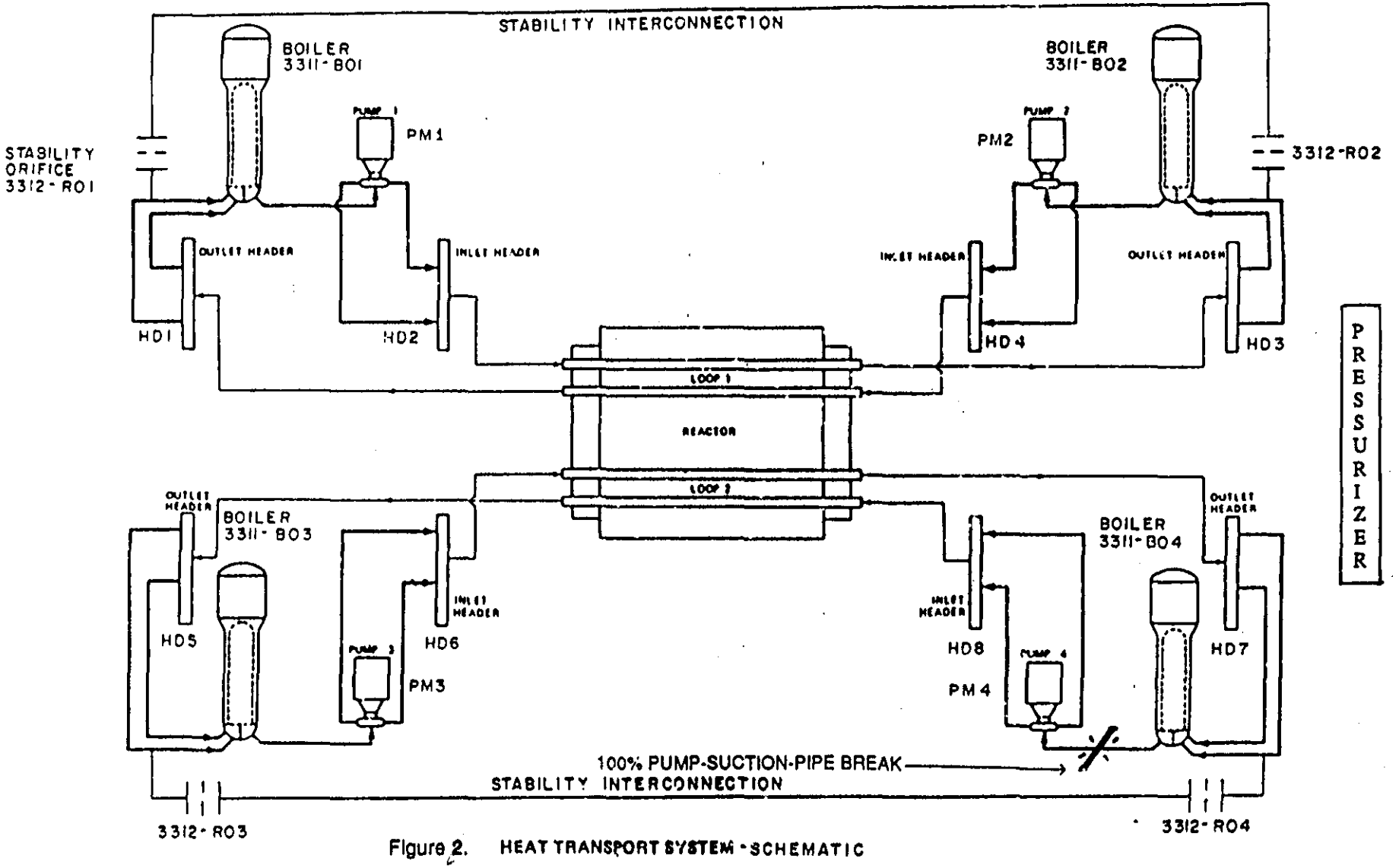

Figure 2. HEAT TRANSPORT SYSTEM - SCHEMATIC

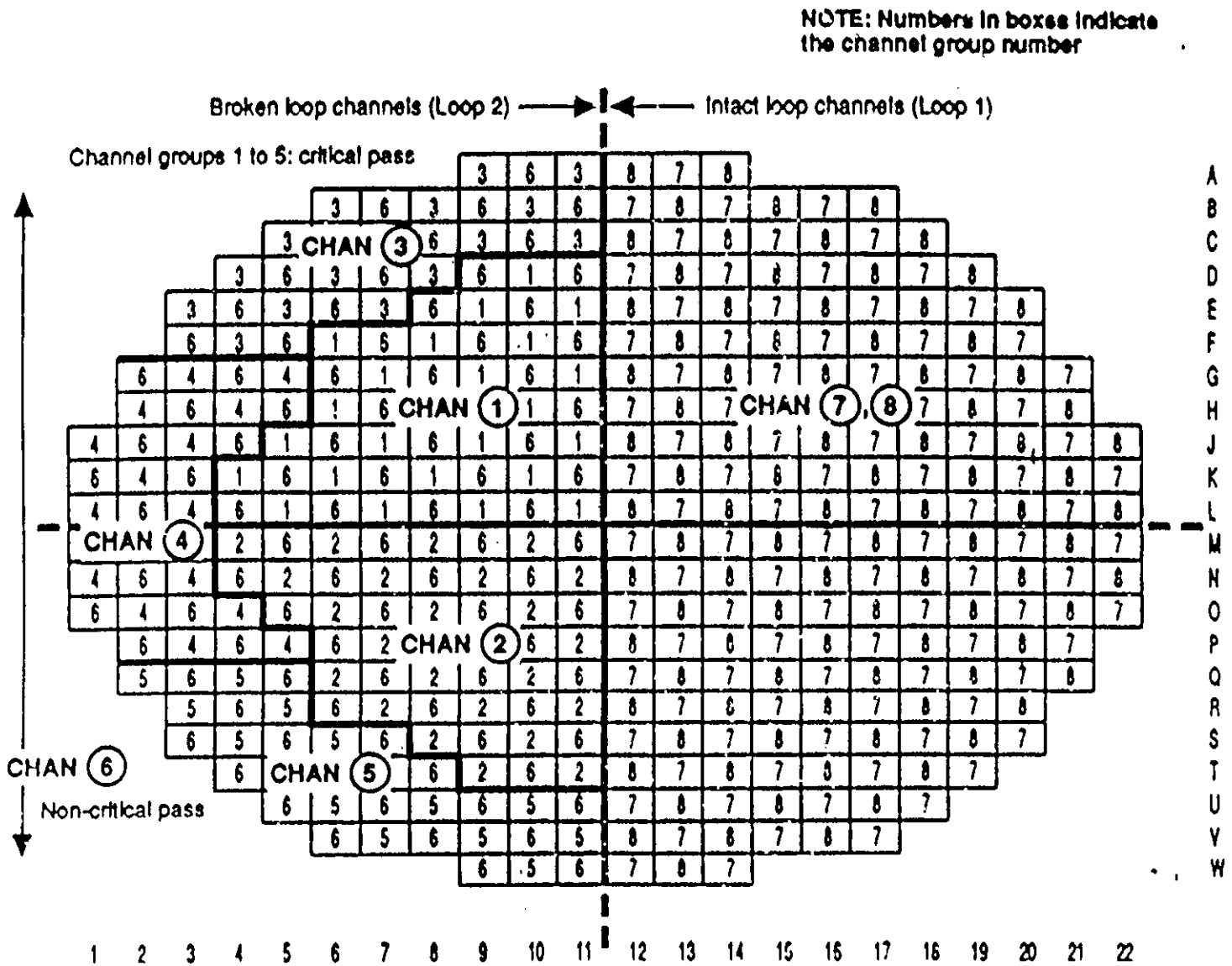

Figure 3. **Thermohydraulic channel group representation**

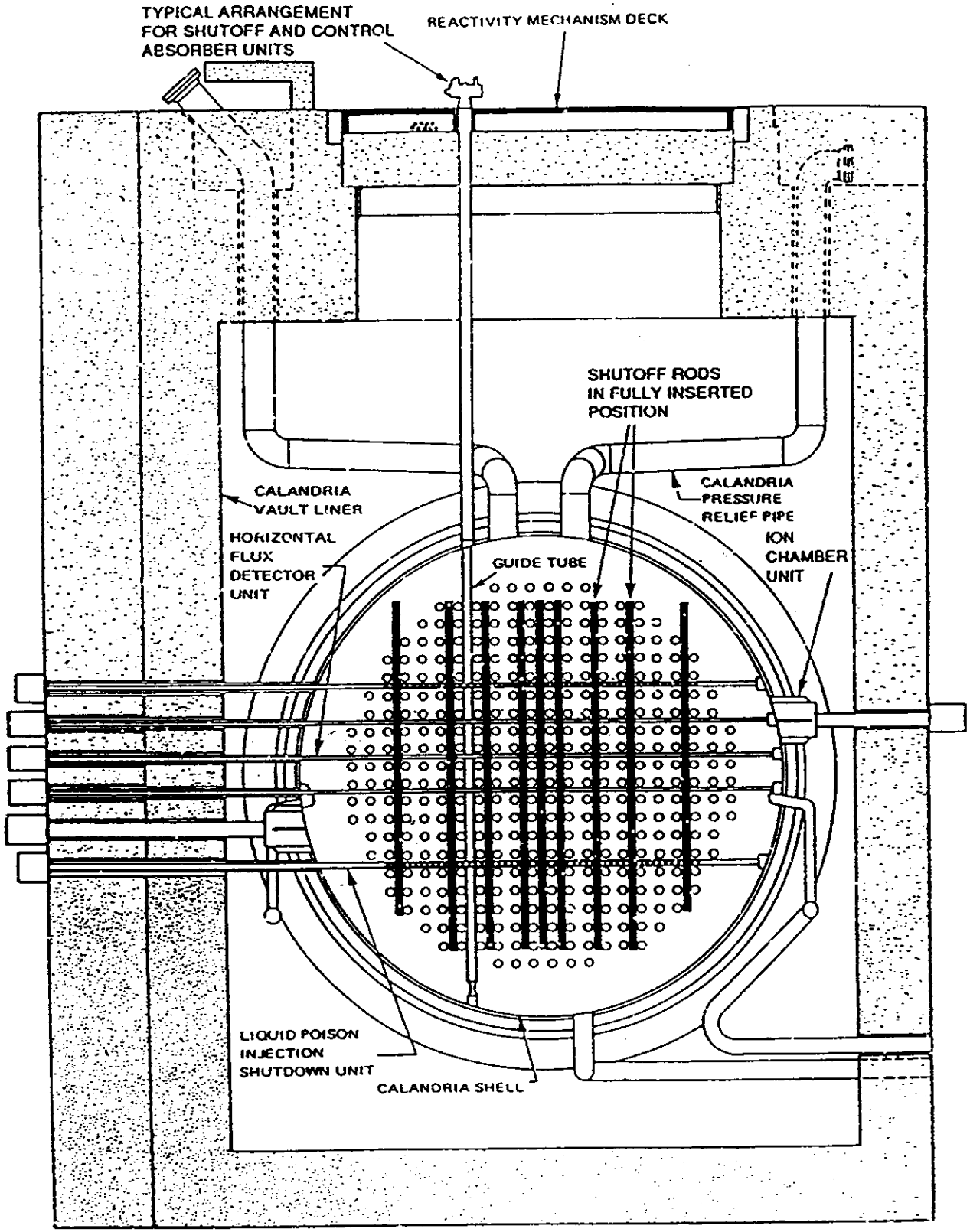

Figure 4a. REACTOR ELEVATION SHOWING SHUTOFF RODS IN FULLY INSERTED POSITION (VIEW FROM PRESSURIZER END)

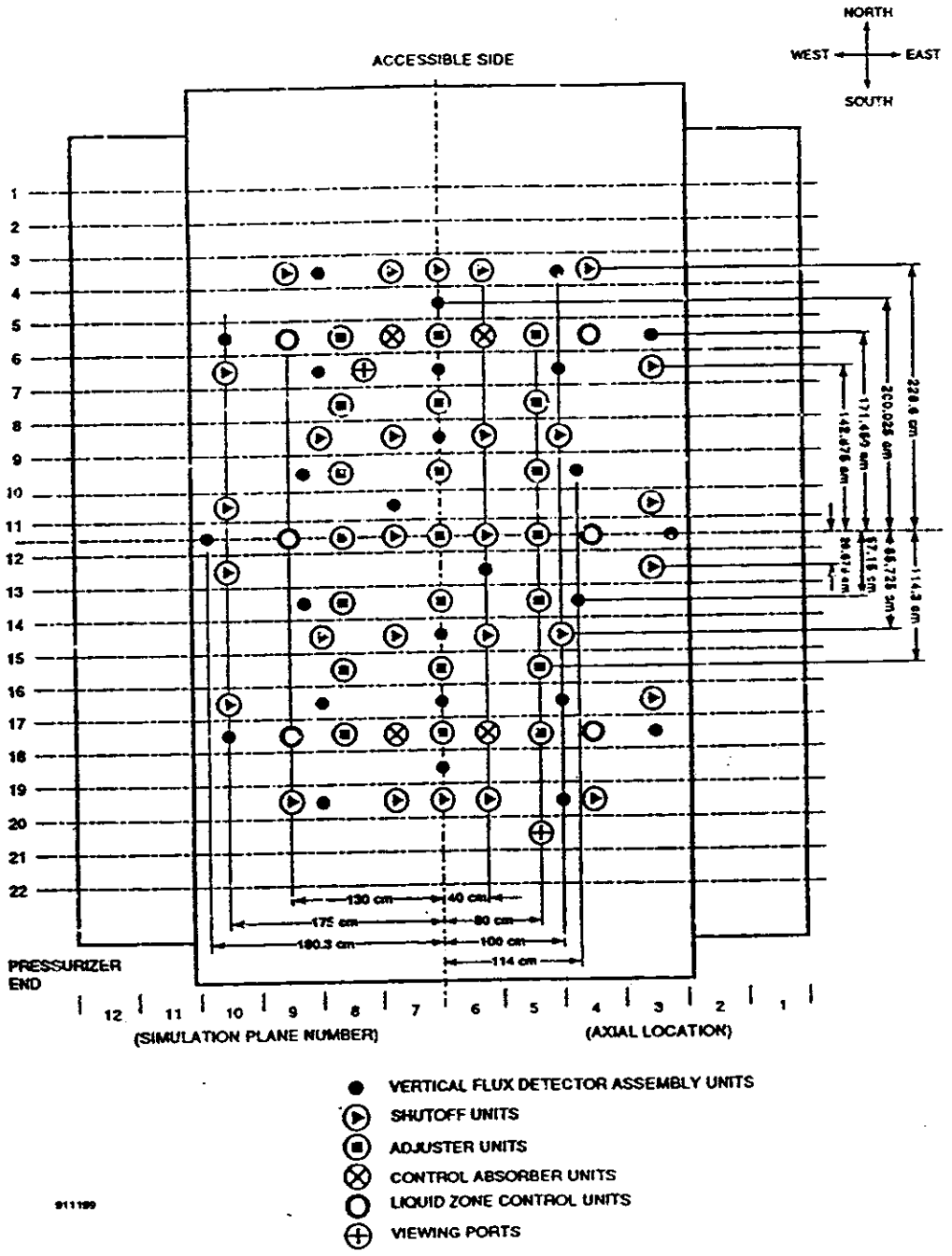

Figure 5.10 Location of Reactivity Devices – Plan View

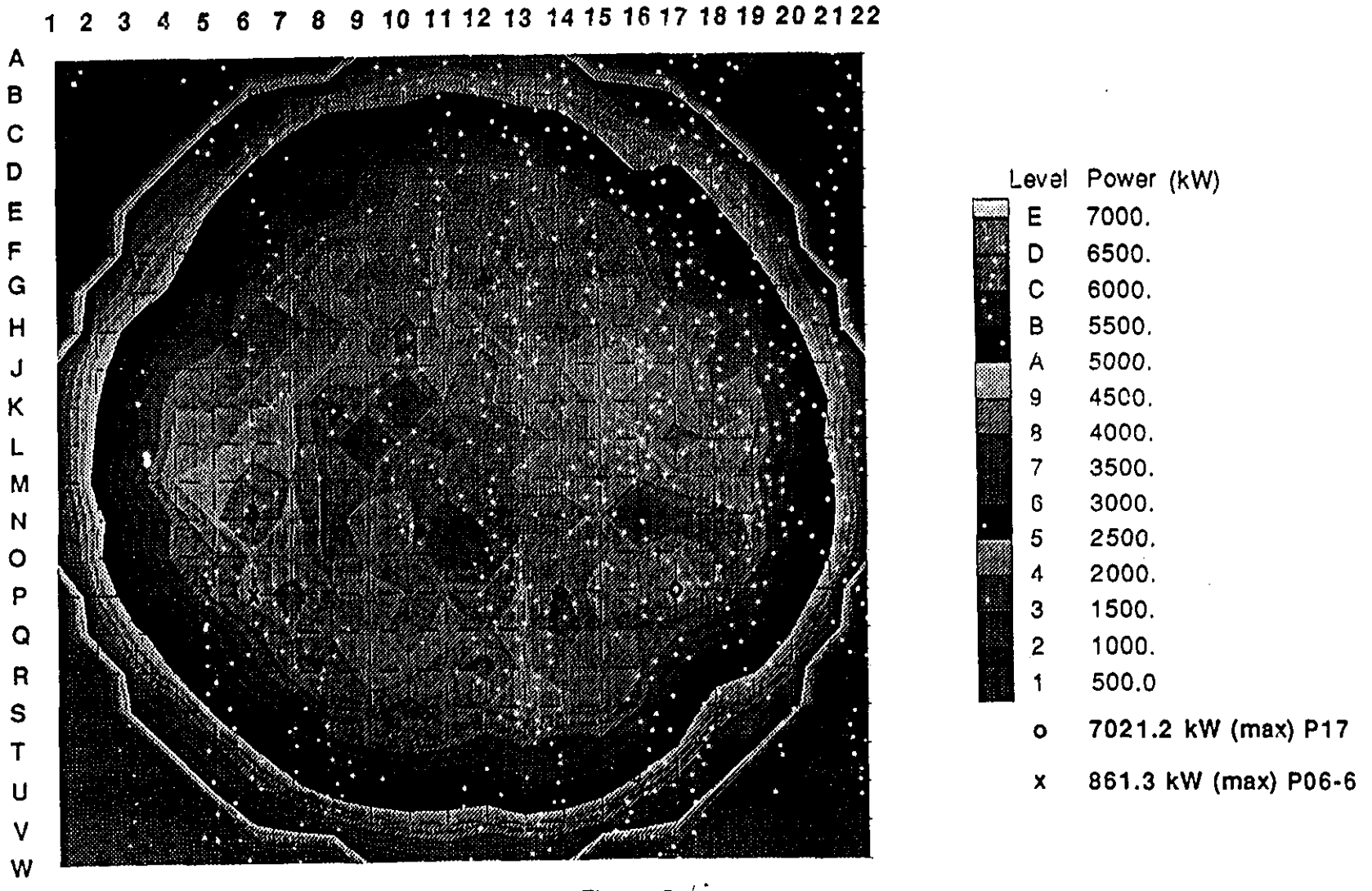

Figure 5.
Pre-LOCA Steady-State Channel Power Distribution in
Point Lepreau Instantaneous Core at 103% FP
(from 2844 FPD flux)

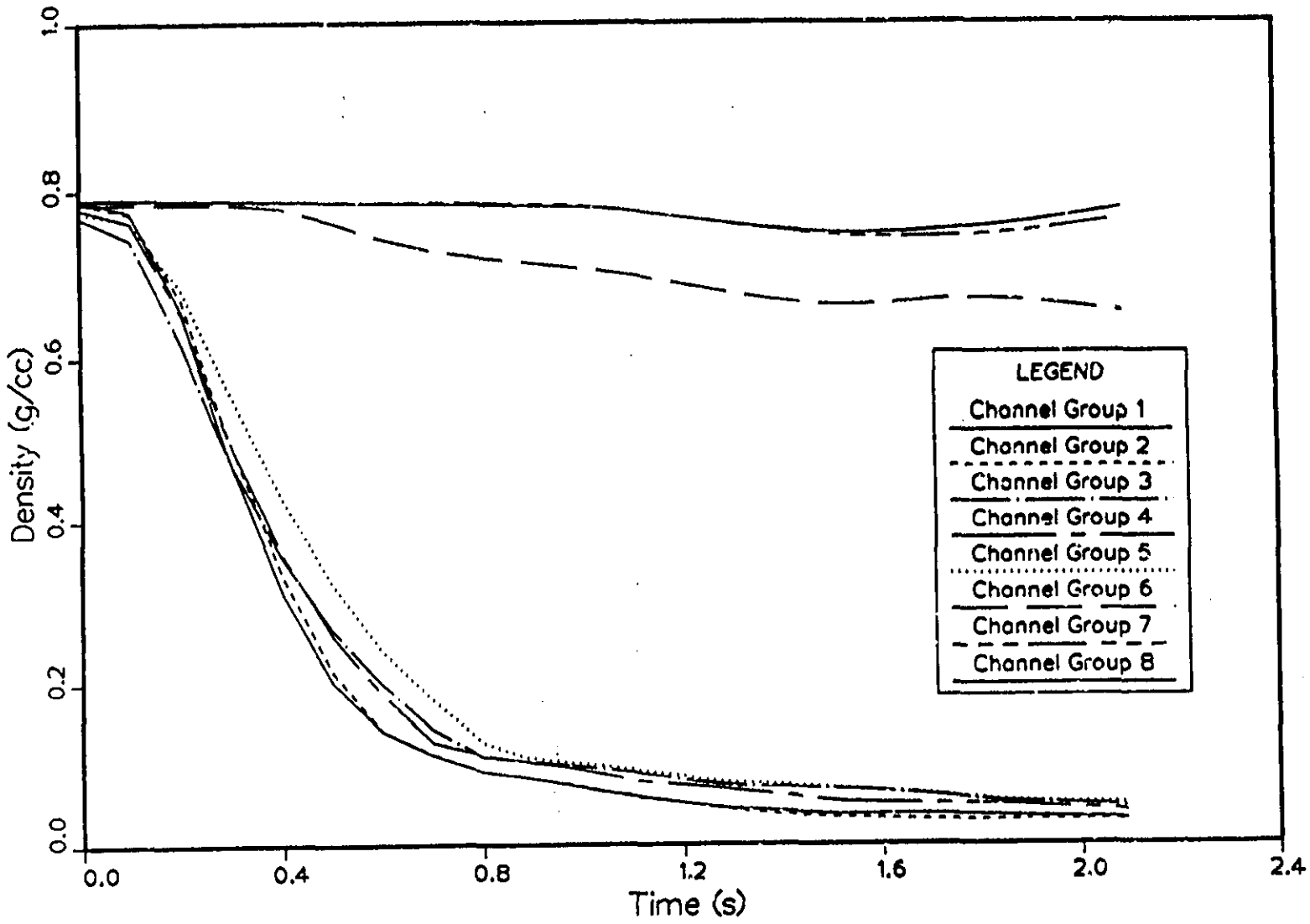

Figure 7. Flux Sq.Wt.Coolant Density 100%PSCR 103%FP No Tilt Lobo

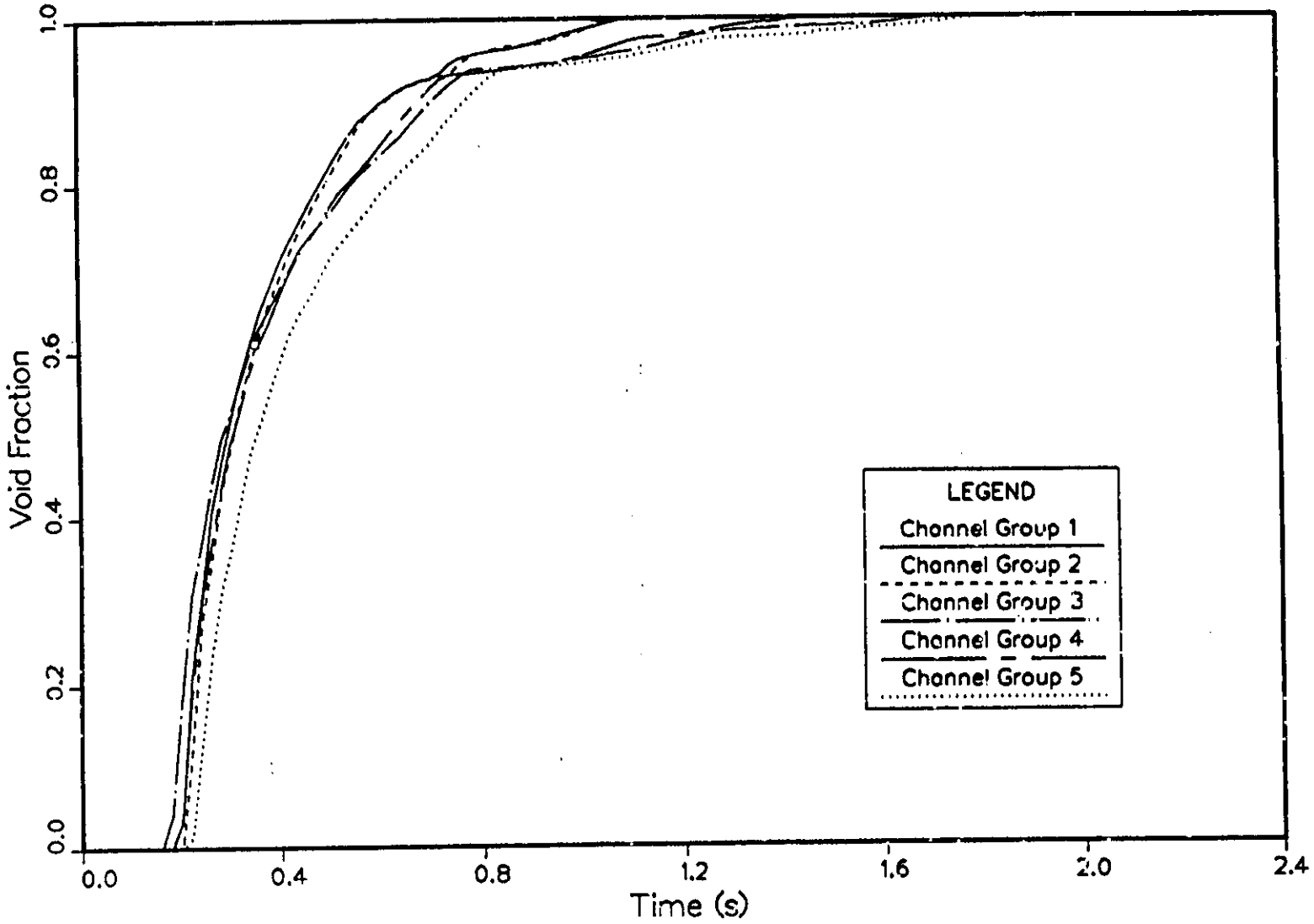

Figure 8. Channel Void Downstream Of Break 100%PSCR 103%FP No Tilt Lobo

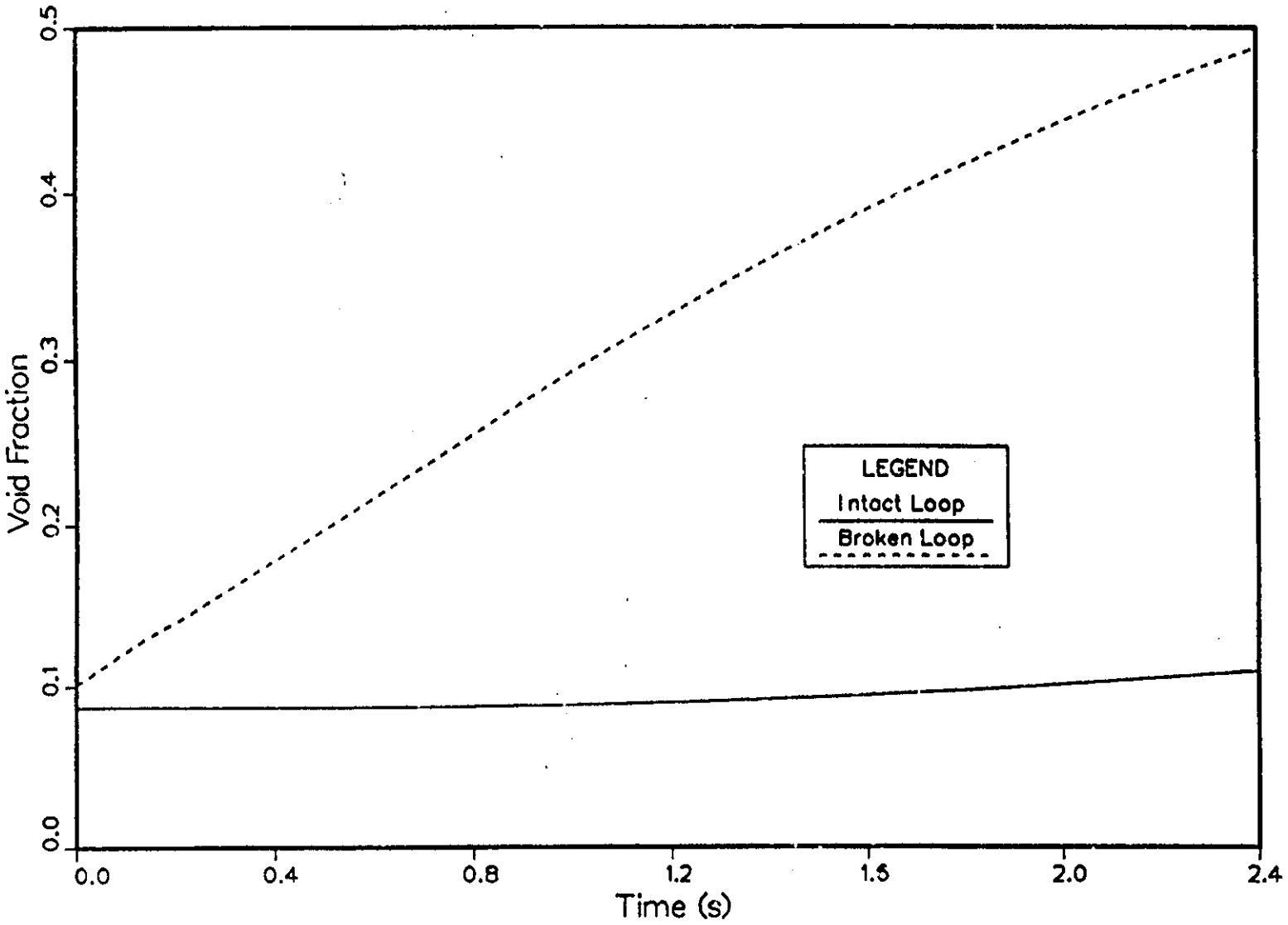

Figure 9. Total Loop Void Fraction 100%PSCR 103%FP No Tilt Lobo

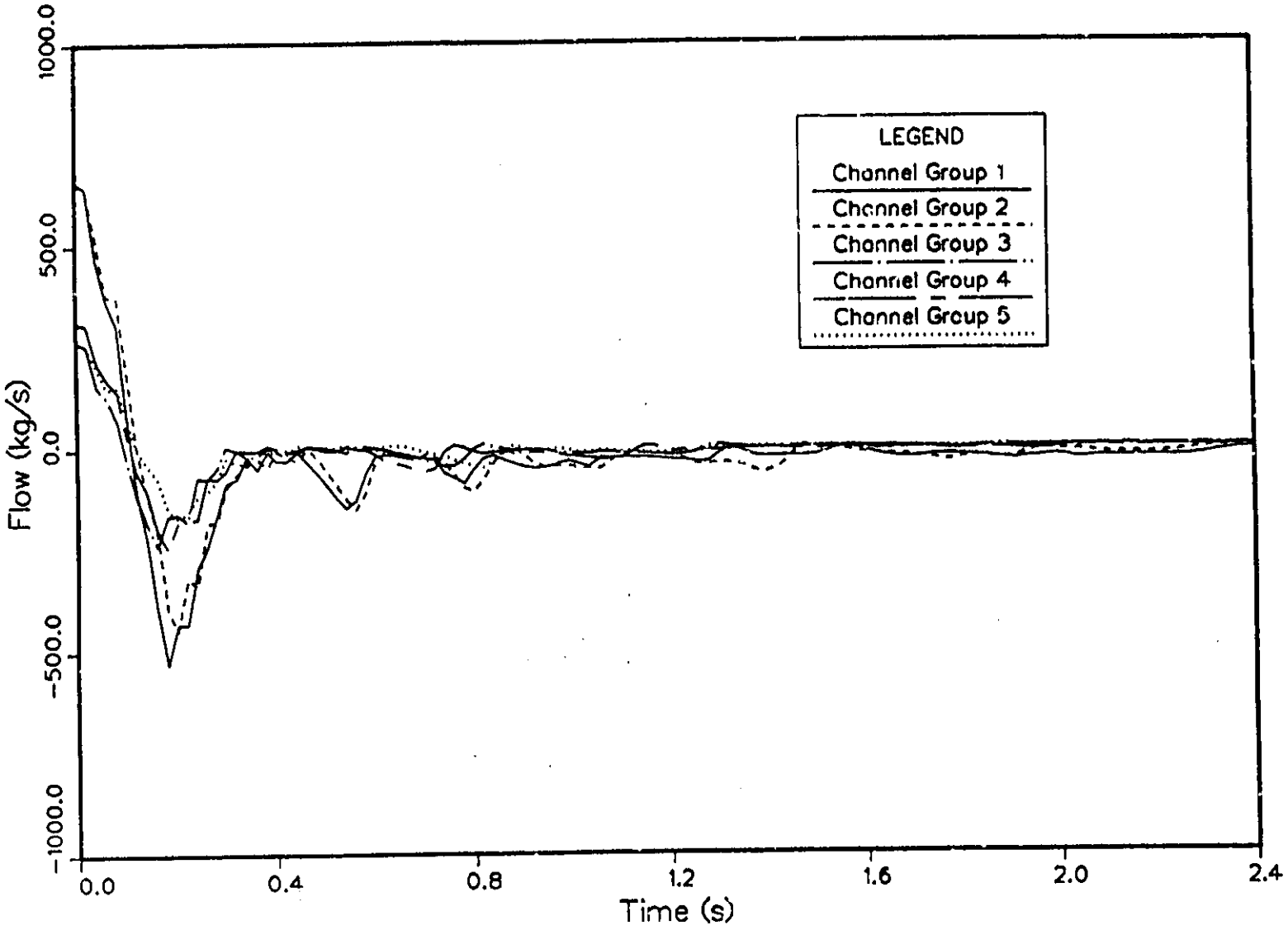

Figure 16. Channel Flows Downstream Of Break 100%PSCR 103%FP No Tilt Lobo

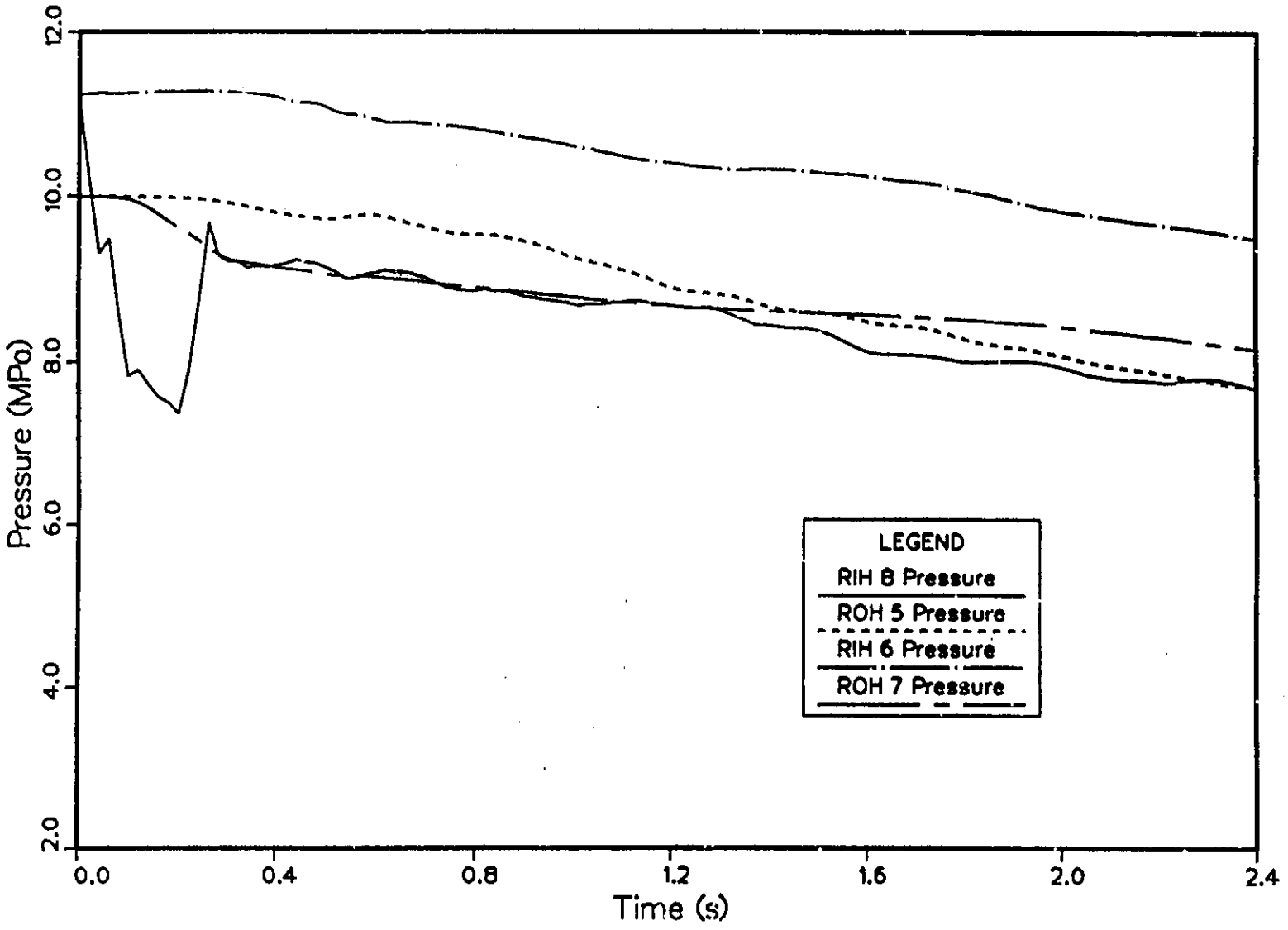

Figure 11. Heoder Pressures In Broken Loop 100%PSCR 103%FP No Tilt Lobo

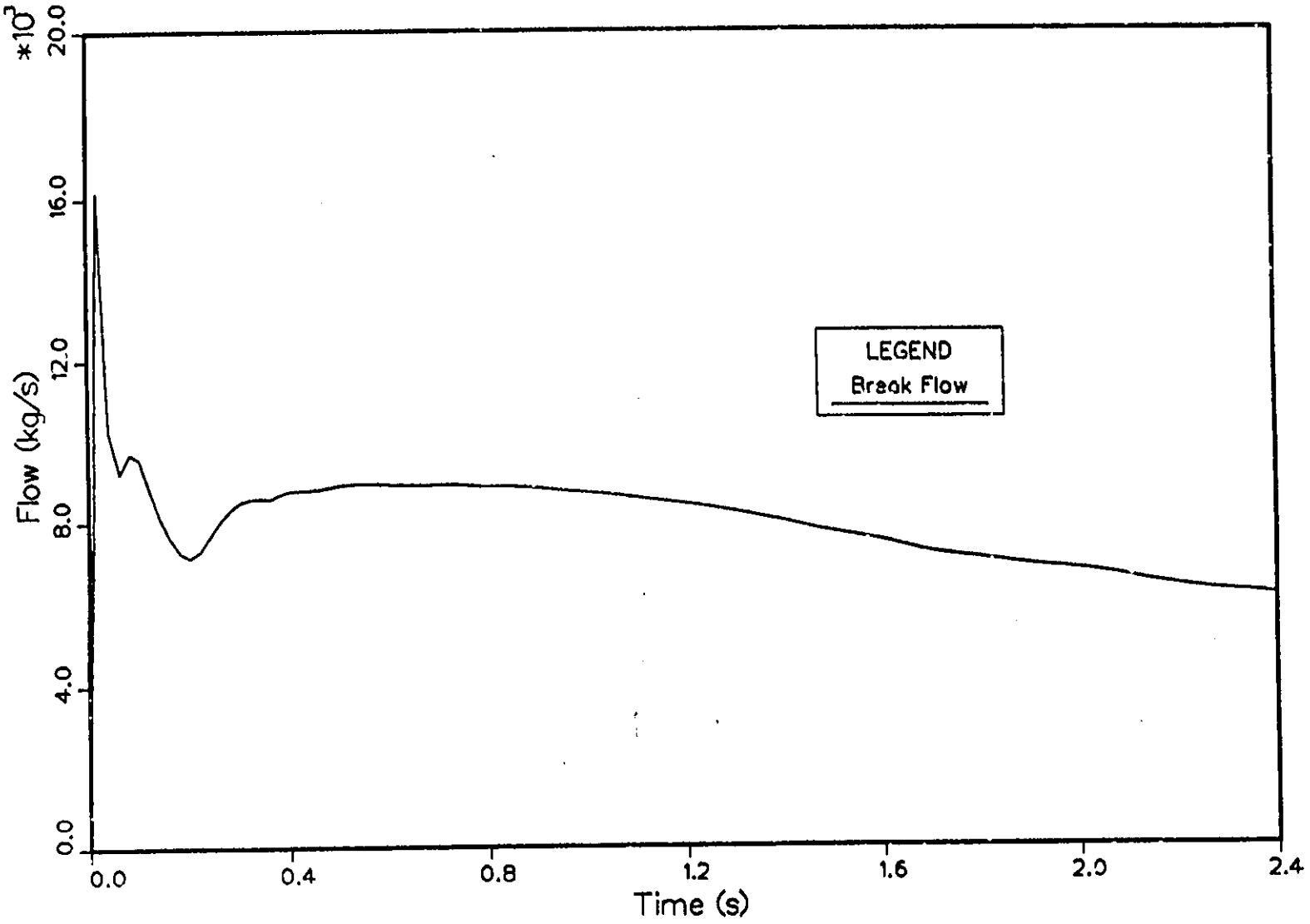

Figure 12. Break Discharge Flow 100%PSCR 103%FP No Tilt Lobo

6.6

Figure 13 -- Positive System Reactivity versus Time in Simulation of 100% PS Break at 103% FP

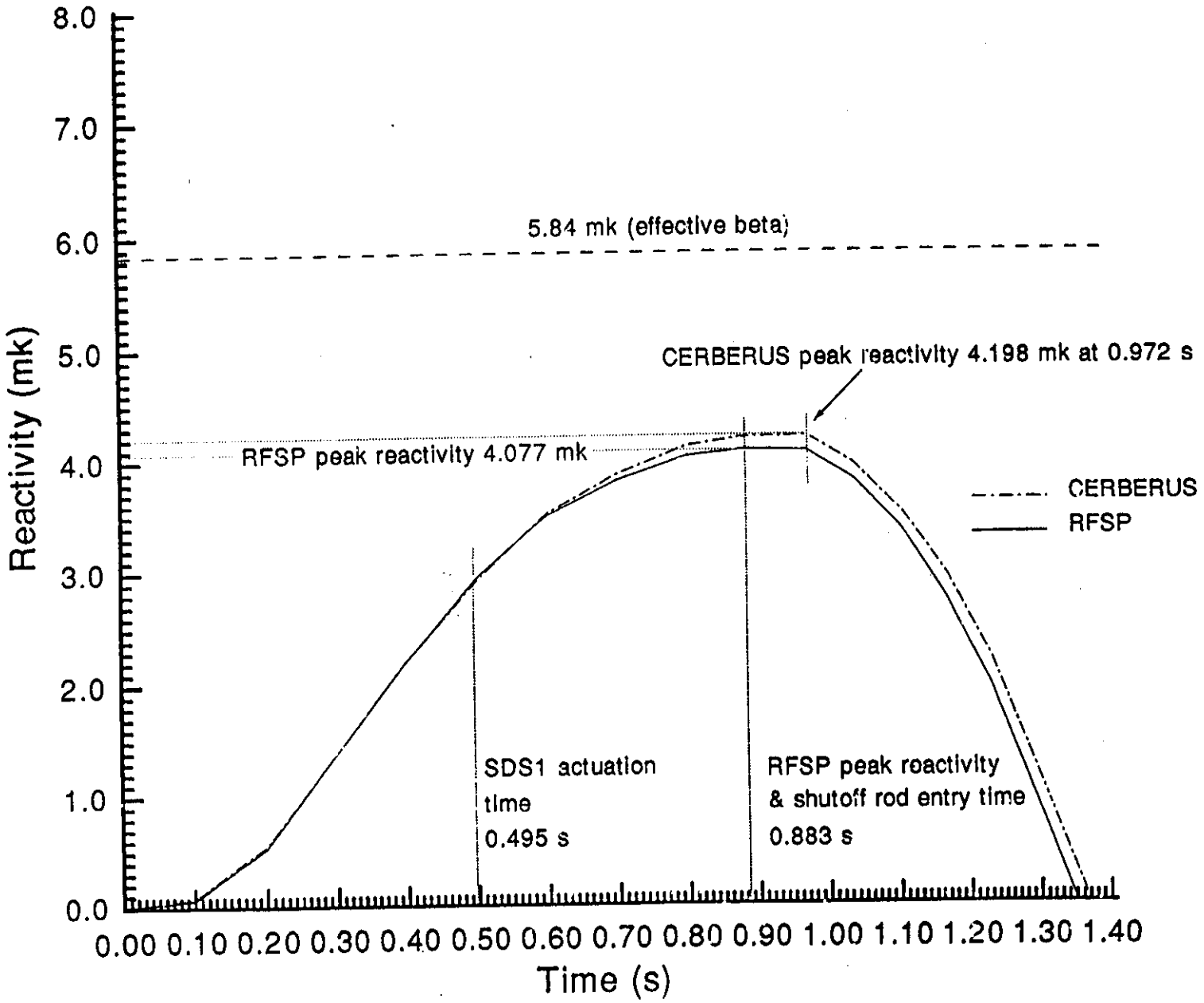

Figure ~~14~~ 6.8 - Total System Reactivity versus Time
in Simulation of 100% PS Break at 103% FP

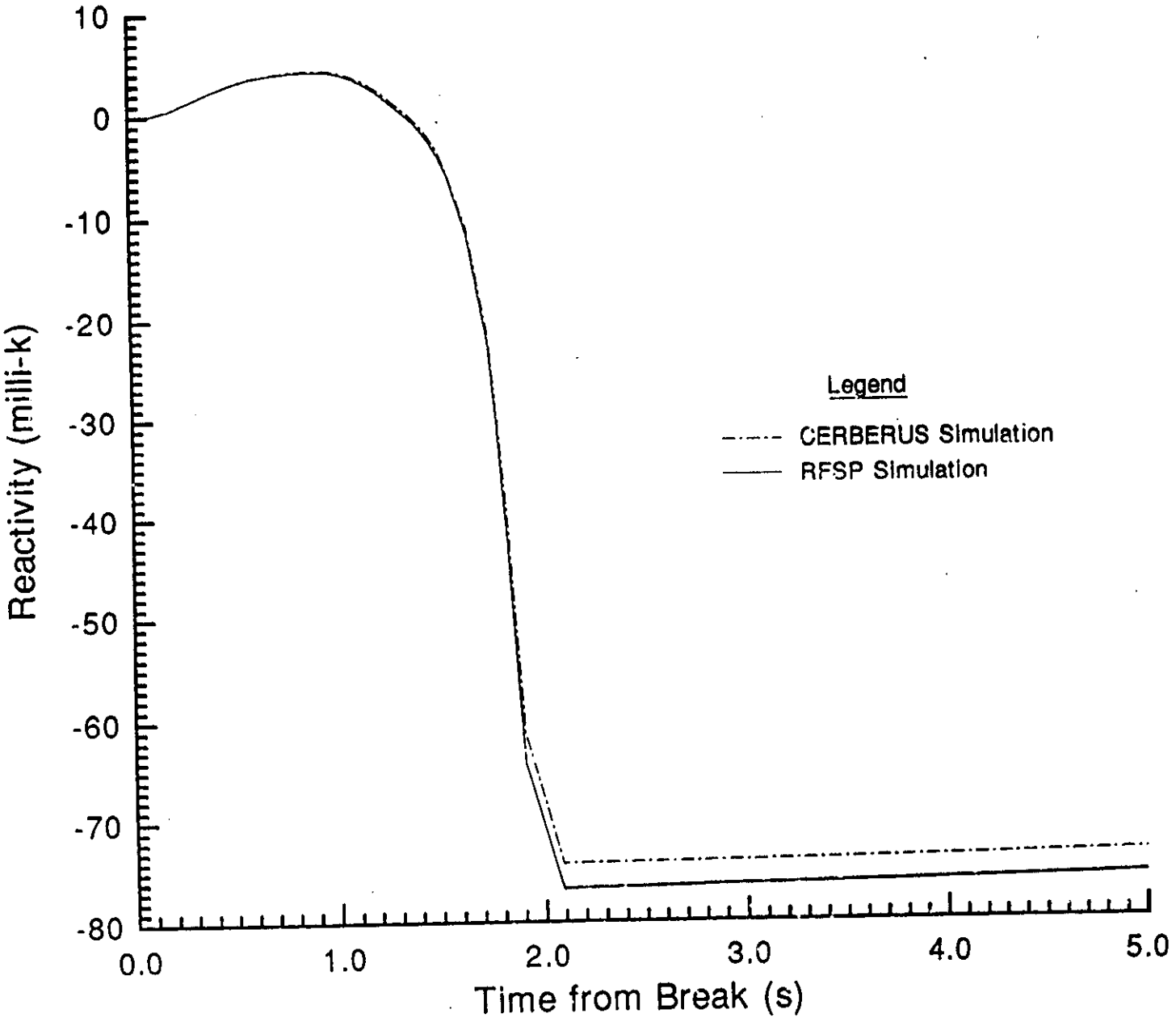

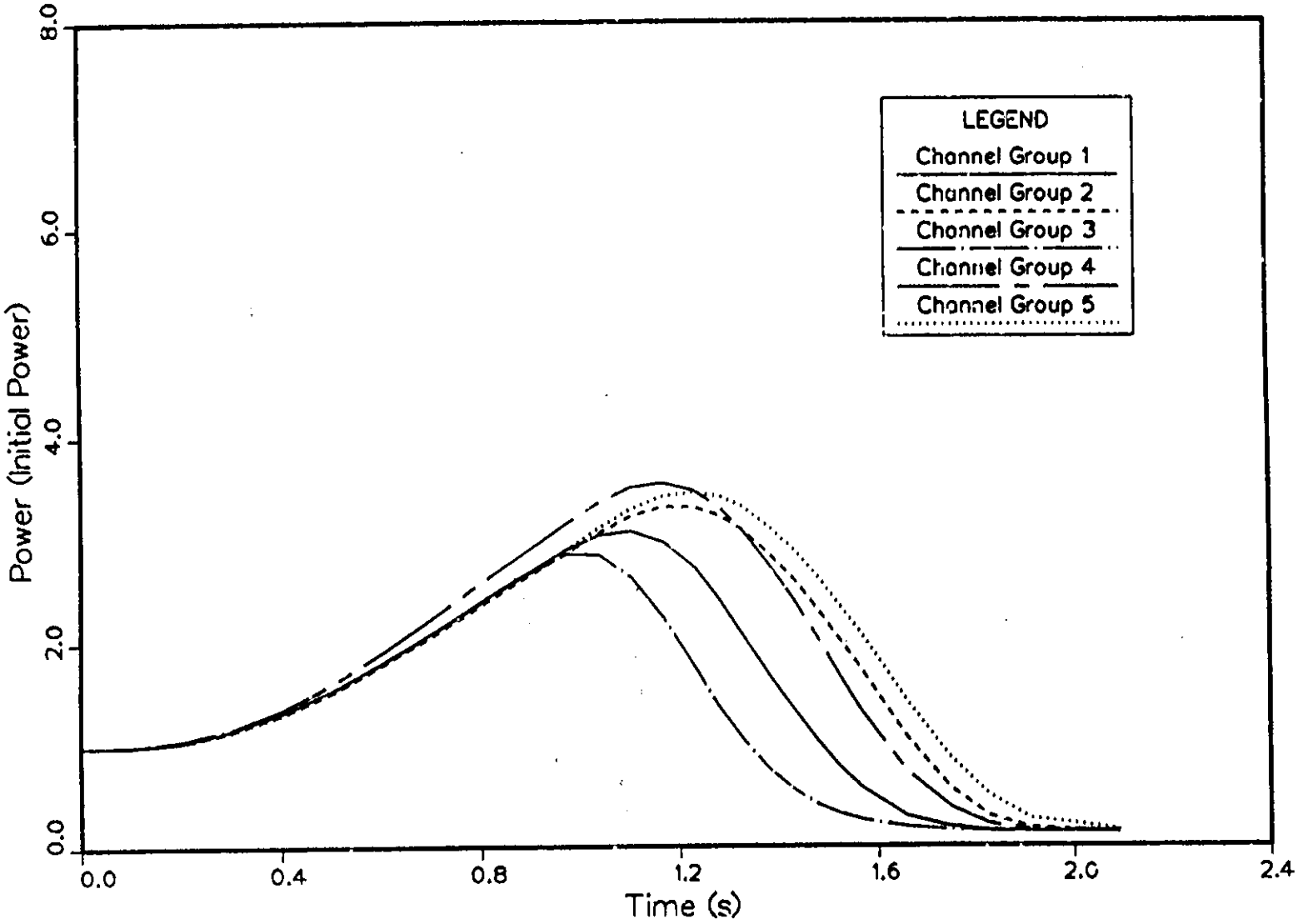

Figure ~~15.~~ 6.9 Axial Center Channel Power 100%PSCR 103%FP No Tilt Lobo

Figure 6.10 -- Relative Powers versus Time in Simulation of 100% PS Break at 103% FP

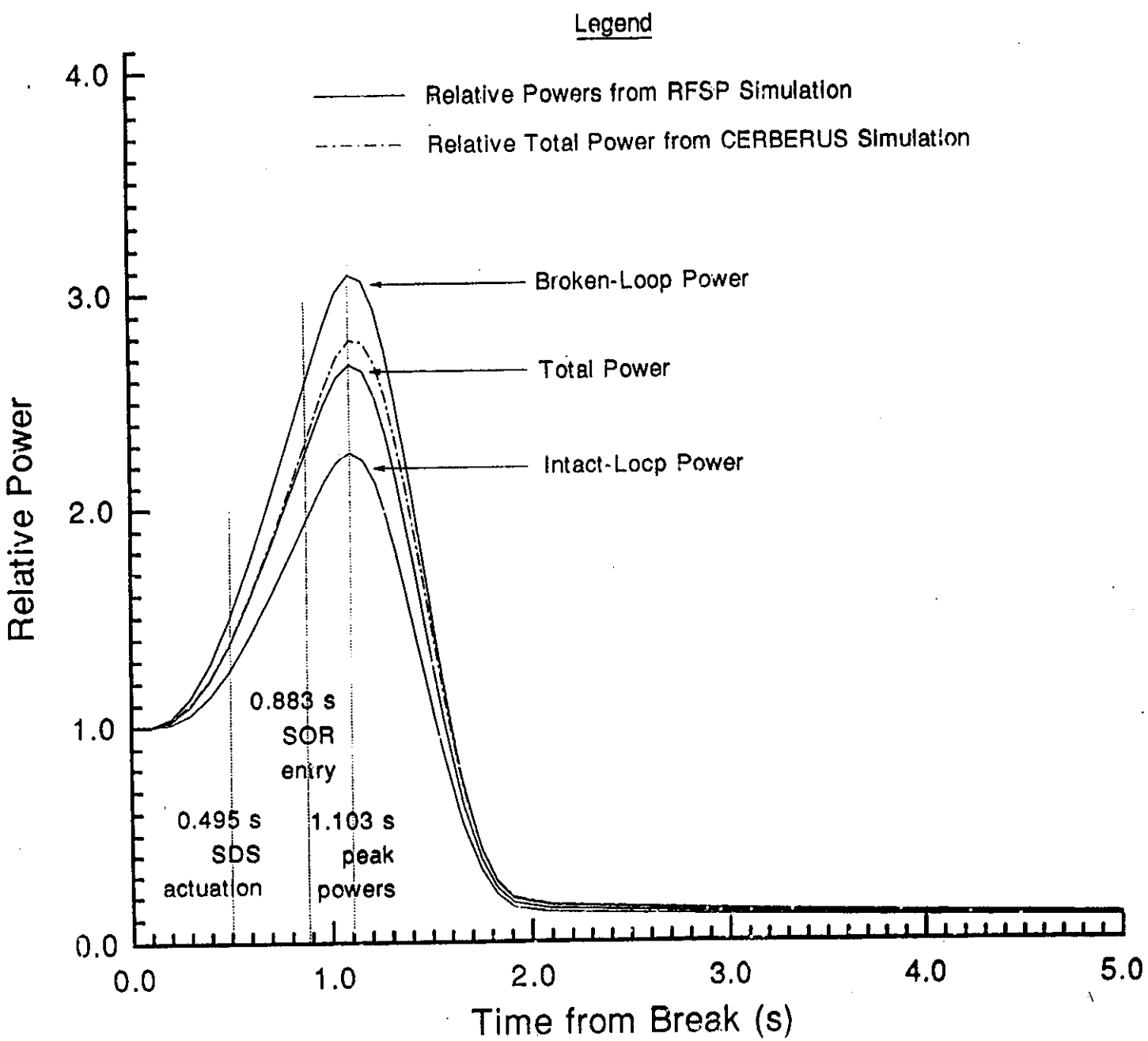

FIGURE 6.11. Power Pulse for Bundles with Highest Stored Energy in Simulation of 100% PS Break at 103% FP

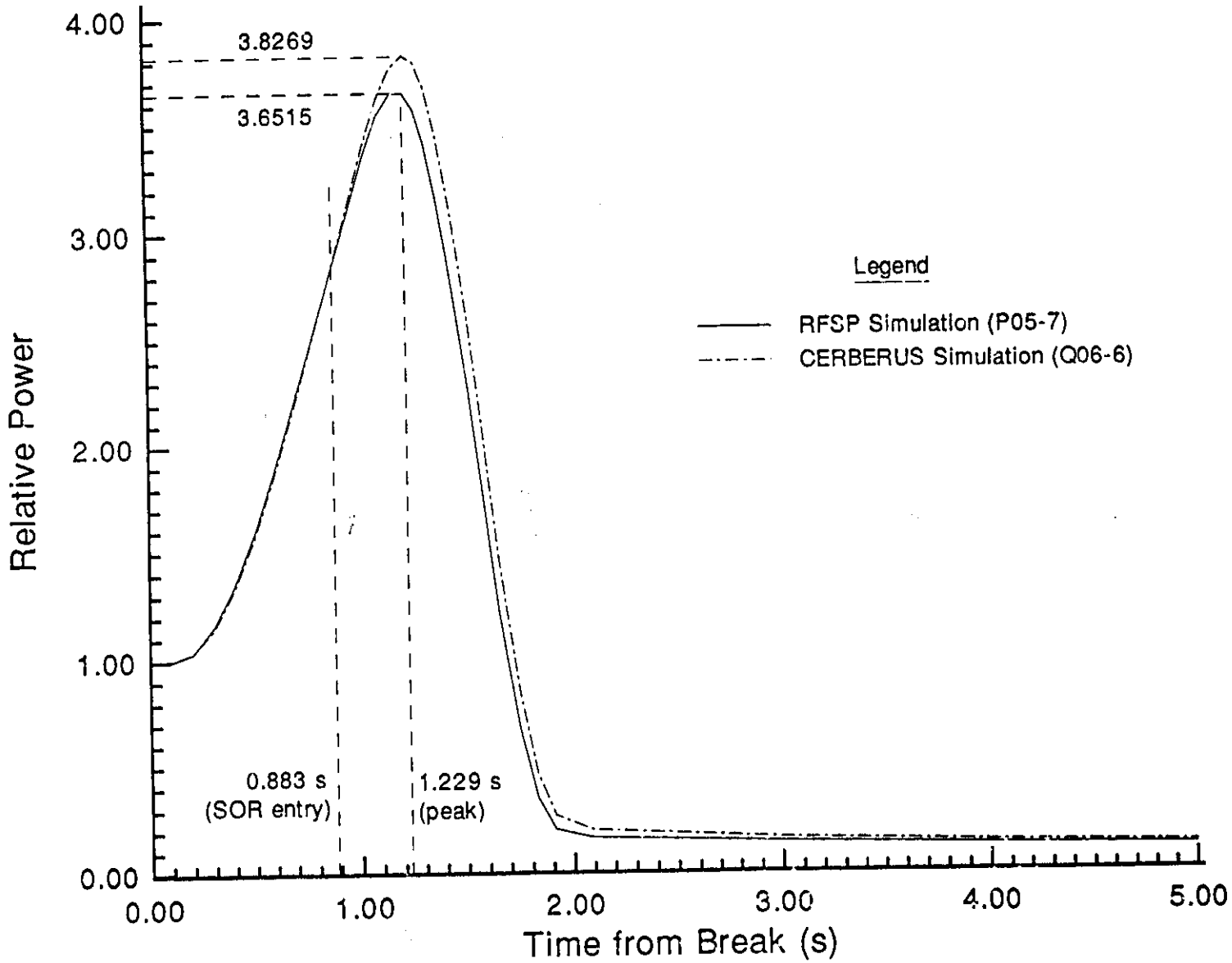

Table 2. Delayed-Neutron Data

	Partial Fraction (β_i)		Time Constant (λ_i) (s^{-1})	
Precursor Group	Instantanteous Model*	Homogeneous Model	Instantaneous Model*	Homogeneous Model
1	$(2.9767\pm0.4188)\times10^{-4}$	2.96×10^{-4}	$(6.1297\pm0.6063)\times10^{-4}$	6.12×10^{-4}
2	$(1.1744\pm0.1625)\times10^{-3}$	1.167×10^{-3}	$(3.1537\pm0.0128)\times10^{-2}$	3.1553×10^{-2}
3	$(1.0421\pm0.1602)\times10^{-3}$	1.036×10^{-3}	0.1221 ± 0.0028	0.1219
4	$(2.3728\pm0.4111)\times10^{-3}$	2.357×10^{-3}	0.3179 ± 0.0032	0.3176
5	$(7.8559\pm1.1969)\times10^{-4}$	7.84×10^{-4}	1.3894 ± 0.0052	1.3982
6	$(1.9727\pm0.2097)\times10^{-4}$	1.99×10^{-4}	3.7807 ± 0.0675	3.7858

Greatest Value of Total Delayed Fraction = 7.8512×10^{-3}
Smallest Value of Total Delayed Fraction = 4.2769×10^{-3}

*Note: The '±' value is 1 standard deviation across the core. The homogeneous values are uniform everywhere.

Fast-Group Velocity	Thermal-Group Velocity
7.648×10^{6} cm/s	0.2708×10^{6} cm/s

Table 3. Times at Which SDS1 Detectors Reach Assumed Setpoints (including times for homogeneous case)

ROP Detectors		Time at Which Trip Setpoint is Reached		Calculation of SDS1 Actuation Time			
Logic Channel	Detector Assembly	CERBERUS Model (s)	RFSP Model (s)	Time at Which Logic Relay Would Clear (s)	Minimum of Previous Column in Each Channel (s)	Time of Actuation of SDS1 (s)	Time Used as Origin of Shutoff-Rod Drop Curve (s)
D	VFD05	0.3370	0.3430	0.3695			
	VFD07	0.4170	0.4220	0.4485			
	VFD08	0.4630	0.4660	0.4925			
	VFD10	0.3350	0.3360	0.3625	0.3625		
	VFD12	0.3490	0.3490	0.3755			
	VFD14	0.4020	0.4030	0.4295			
	VFD15	0.4380	0.4370	0.4635			
	VFD17	0.4890	0.4880	0.5145			
	VFD20	0.3790	0.3750	0.4015			
	VFD20	0.3910	0.3880	0.4145			
	VFD21	0.4250	0.4200	0.4465			
	VFD22	0.4670	0.4650	0.4915			
E	VFD05	0.3260	0.3330	0.3595	0.3595		
	VFD06	0.3630	0.3700	0.3965			
	VFD07	0.4070	0.4110	0.4375			
	VFD07	0.4120	0.4190	0.4455			
	VFD10	0.3340	0.3350	0.3615			
	VFD12	0.3690	0.3680	0.3945			
	VFD15	0.4300	0.4280	0.4545			
	VFD17	0.4850	0.4860	0.5125			
	VFD19	0.3680	0.3650	0.3915			
	VFD21	0.4310	0.4270	0.4535			
	VFD25	0.4150	0.4080	0.4345			
F	VFD02	0.3790	0.3930	0.4195			
	VFD06	0.3440	0.3530	0.3795			
	VFD06	0.3440	0.3560	03825			
	VFD08	0.4590	0.4630	0.4895			
	VFD10	0.3430	0.3430	0.3695	0.3695		
	VFD13	0.3860	0.3830	0.4095			
	VFD17	0.4810	0.4810	0.5075			
	VFD19	0.3590	0.3560	0.3825			
	VFD20	0.3750	0.3720	0.3985			
	VFD21	0.4340	0.4300	0.4555			
	VFD22	0.4710	0.4680	0.4945			

Table 3. (continued)

Ion Chambers		Time at Which Trip Setpoint is Reached		Calculation of SDS1 Actuation Time			
Logic Channel	Detector Assembly	CERBERUS Model (s)	RFSP Model (s)	Time at Which Logic Relay Would Clear (s)	Minimum of Previous Column in Each Channel (s)	Time of Actuation of SDS1 (s)	Time Used as Origin of Shutoff-Rod Drop Curve (s)
D	IC1	0.4570	0.4560	0.4950	0.4950		
E	IC2	0.4550	0.4560	0.4950	0.4950	0.4950	0.5110
F	IC3	0.4520	0.4530	0.4920	0.4920		

Note: The SDS actuation time in the homogeneous case (Reference 3) was found to be 1 ms later than the one calculated here; i.e. the time of actuation of SDS1 was 0.496 s in the homogeneous model.

Table 4. Reactivity vs Time (including reactivity from homogeneous case)

Case Number	Time* (s)	Homogeneous Model**	Instantaneous Model	
		Reactivity (mk)	Reactivity (mk)	Effective β ($\times 10^{-3}$)
1	0.000	0.0000	0.000	–
3	0.100	0.0700	0.057	5.840
4	0.200	0.5565	0.536	5.840
5	0.300	1.3824	1.383	5.840
6	0.400	2.2051	2.202	5.841
7	0.500	2.9082	2.936	5.842
8	0.600	3.5068	3.485	5.842
9	0.700	3.8617	3.806	5.843
10	0.800	4.1124	4.022	5.843
11	0.883	4.1896	4.077	5.843
12	0.972	4.1978	4.064	5.843
13	1.037	3.9426	3.805	5.842
14	1.103	3.5086	3.358	5.842
15	1.169	2.9271	2.719	5.841
16	1.229	2.2130	1.969	5.840
17	1.280	1.4201	1.149	5.840
18	1.329	0.6116	0.338	5.840
19	1.380	–0.1997	–0.491	5.839
20	1.429	–1.1498	–1.500	5.840
21	1.476	–2.3385	–2.697	5.841
22	1.521	–3.7857	–4.208	5.842
23	1.564	–5.9218	–6.049	5.844
24	1.655	–11.2021	–11.811	5.852
25	1.750	–21.5348	–22.472	5.862
26	1.827	–38.8496	–40.867	5.864
27	1.910	–61.4535	–64.335	5.852
28	2.088	–74.2230	–76.764	5.841
29	3.000	–74.0341	–76.462	5.841
30	4.000	–73.7474	–76.093	5.841
31	5.000	–73.3445	–75.638	5.842

* Note that the times for the homogeneous model are actually 1 ms later than the times for the instantaneous model for cases 11 - 28. Thus, for example, case 11 is at 0.883 s for the instantaneous model and at 0.884 s for the homogeneous model.

** The effective β was assumed to be a constant value of 5.84×10^{-3} at all times.

Table 5. Relative Powers vs Time (including results from homogeneous case)

		Total Relative Power		Broken Loop Relative Power (Low x)		Intact Loop Relative Power (High x)		Relative Powers over Other Core Halves			
Case No.	Time* (s)	Inst. Model	Hom. Model	Inst. Model	Hom. Model	Inst. Model	Hom. Model	Low y	High y	Low z	High z
1	0.000	1.0000	1.0000	1.0000	1.0000	1.0000	1.0000	1.0000	1.0000	1.0000	1.0000
3	0.100	1.0026	1.0034	1.0037	1.0055	1.0014	1.0013	1.0026	1.0025	1.0036	1.0015
4	0.200	1.0263	1.0303	1.0391	1.0457	1.0135	1.0152	1.0279	1.0247	1.0342	1.0184
5	0.300	1.0944	1.1041	1.1326	1.1471	1.0562	1.0617	1.0983	1.0905	1.1060	1.0827
6	0.400	1.2131	1.2315	1.2869	1.3127	1.1393	1.1513	1.2191	1.2071	1.2176	1.2085
7	0.500	1.3789	1.4076	1.4982	1.5364	1.2596	1.2804	1.3865	1.3713	1.3690	1.3888
8	0.600	1.5855	1.6301	1.7571	1.8162	1.4140	1.4461	1.5940	1.5770	1.5599	1.6112
9	0.700	1.8190	1.8882	2.0455	2.1356	1.5927	1.6437	1.8297	1.8084	1.7779	1.8603
10	0.800	2.0674	2.1694	2.3479	2.4797	1.7870	1.8627	2.0797	2.0552	2.0120	2.1231
11	0.883	2.2756	2.4134	2.5972	2.7731	1.9541	2.0578	2.2886	2.2627	2.2100	2.3416
12	0.972	2.4879	2.6653	2.8512	3.0750	2.1248	2.2603	2.4958	2.4801	2.4116	2.5646
13	1.037	2.6137	2.8201	3.0056	3.2642	2.2219	2.3812	2.5843	2.6431	2.5302	2.6977
14	1.103	2.6744	2.9050	3.0858	3.3743	2.2632	2.4411	2.5676	2.7810	2.5860	2.7633
15	1.169	2.6427	2.8927	3.0585	3.3729	2.2270	2.4180	2.4243	2.8605	2.5535	2.7323
16	1.229	2.5249	2.7856	2.9290	3.2601	2.1210	2.3167	2.1867	2.8622	2.4395	2.6108
17	1.280	2.3577	2.6176	2.7407	3.0731	1.9748	2.1673	1.9133	2.8010	2.2790	2.4368
18	1.329	2.1505	2.3982	2.5045	2.8222	1.7966	1.9792	1.6209	2.6788	2.0811	2.2203
19	1.380	1.9120	2.1369	2.2281	2.5180	1.5959	1.7602	1.3285	2.4939	1.8534	1.9708
20	1.429	1.6749	1.8731	1.9516	2.2083	1.3983	1.5417	1.0674	2.2808	1.6277	1.7223
21	1.476	1.4455	1.6132	1.6826	1.9016	1.2085	1.3282	0.8408	2.0487	1.4095	1.4817
22	1.521	1.2284	1.3633	1.4280	1.6059	1.0288	1.1235	0.6490	1.8063	1.2033	1.2536
23	1.564	1.0280	1.1208	1.1921	1.3183	0.8638	0.9256	0.4942	1.5603	1.0129	1.0431
24	1.655	0.6494	0.6742	0.7452	0.7916	0.5535	0.5581	0.2813	1.0164	0.6502	0.6485
25	1.750	0.3793	0.3592	0.4295	0.4226	0.3292	0.2966	0.1883	0.5698	0.3869	0.3717
26	1.827	0.2413	0.1993	0.2711	0.2366	0.2115	0.1622	0.1573	0.3251	0.2505	0.2320
27	1.910	0.1720	0.1178	0.1922	0.1423	0.1519	0.0936	0.1445	0.1995	0.1806	0.1634
28	2.088	0.1456	0.0869	0.1617	0.1059	0.1294	0.0681	0.1403	0.1508	0.1532	0.1379
29	3.000	0.1254	0.0664	0.1375	0.0807	0.1132	0.0523	0.1228	0.1279	0.1315	0.1192
30	4.000	0.1128	0.0548	0.1227	0.0664	0.1028	0.0433	0.1110	0.1145	0.1180	0.1075
31	5.000	0.1040	0.0471	0.1125	0.0570	0.0955	0.0372	0.1026	0.1054	0.1086	0.0994

* The homogeneous model times are 1 ms later than the times for the instantaneous model from cases 11 - 28.

Table 6. Tilts in Three Spatial Directions vs Time

Case Number	Time (s)	Horizontal Power Tilt (%)	Vertical Power Tilt (%)	Axial Power Tilt (%)
1	0.000	–0.02	0.13	–0.26
3	0.100	0.10	0.13	–0.36
4	0.200	1.23	–0.02	–1.02
5	0.300	3.47	–0.23	–1.32
6	0.400	6.06	–0.36	–0.63
7	0.500	8.63	–0.42	0.46
8	0.600	10.80	–0.41	1.36
9	0.700	12.43	–0.45	2.01
10	0.800	13.55	–0.46	2.43
11	0.883	14.11	–0.44	2.64
12	0.972	14.58	–0.19	2.82
13	1.037	14.97	1.26	2.95
14	1.103	15.36	4.12	3.06
15	1.169	15.71	8.38	3.13
16	1.229	15.98	13.51	3.14
17	1.280	16.22	18.96	3.09
18	1.329	16.44	24.73	2.98
19	1.380	16.51	30.61	2.81
20	1.429	16.50	36.36	2.57
21	1.476	16.38	41.91	2.24
22	1.521	16.23	47.24	1.79
23	1.564	15.95	51.99	1.22
24	1.655	14.74	56.73	–0.38
25	1.750	13.21	50.42	–2.26
26	1.827	12.33	34.90	–4.09
27	1.910	11.71	16.12	–5.26
28	2.088	11.06	3.75	–5.54
29	3.000	9.68	2.15	–5.16
30	4.000	8.80	1.70	–4.90
31	5.000	8.16	1.44	–4.66

Table 7. Relative Power vs Time for Bundle with Highest Stored Energy at End of Transient for Both Instantaneous and Homogeneous Cases

		Relative Bundle Power	
Case Number	Time* (s)	Instant. Model (P05-7)	Homog. Model (Q06-6)
1	0.000	1.0000	1.0000
3	0.100	1.0029	1.0034
4	0.200	1.0369	1.0385
5	0.300	1.1612	1.1482
6	0.400	1.3476	1.3318
7	0.500	1.5913	1.5680
8	0.600	1.8891	1.8642
9	0.700	2.2217	2.1941
10	0.800	2.5620	2.5501
11	0.883	2.8416	2.8528
12	0.972	3.1333	3.1690
13	1.037	3.3540	3.4062
14	1.103	3.5417	3.6211
15	1.169	3.6481	3.7715
16	1.229	3.6515	3.8269
17	1.280	3.5714	3.7964
18	1.329	3.4109	3.6784
19	1.380	3.1669	3.4657
20	1.429	2.8853	3.2044
21	1.476	2.5800	2.9091
22	1.521	2.2627	2.5895
23	1.564	1.9408	2.2440
24	1.655	1.2378	1.4812
25	1.750	0.6661	0.8395
26	1.827	0.3478	0.4608
27	1.910	0.2023	0.2684
28	2.088	0.1629	0.1990
29	3.000	0.1367	0.1563
30	4.000	0.1213	0.1355
31	5.000	0.1109	0.1223

* The homogeneous model times are 1 ms later than the times for the instantaneous model from cases 11 - 28.